Chebyshev matrix product state impurity solver for dynamical mean-field theory

F. Alexander Wolf, Ian P. Mcculloch, Olivier Parcollet, Ulrich Schollwöck

Chebyshev Matrix Product State Impurity Solver for the Dynamical Mean-Field Theory

F. Alexander Wolf,[1] Ian P. McCulloch,[2] Olivier Parcollet,[3] and Ulrich Schollwöck[1]

[1] *Theoretical Nanophysics, Arnold Sommerfeld Center for Theoretical Physics, LMU München, Theresienstrasse 37, D-80333 München, Germany*
[2] *Centre for Engineered Quantum Systems, School of Physical Sciences, The University of Queensland, Brisbane, Queensland 4072, Australia*
[3] *Institut de Physique Théorique, CEA, IPhT, CNRS, URA 2306, F-91191 Gif-sur-Yvette, France*

(Dated: July 8, 2014)

We compute the spectral functions for the two-site dynamical cluster theory and for the two-orbital dynamical mean-field theory in the density-matrix renormalization group (DMRG) framework using Chebyshev expansions represented with matrix product states (MPS). We obtain quantitatively precise results at modest computational effort through technical improvements regarding the truncation scheme and the Chebyshev rescaling procedure. We furthermore establish the relation of the Chebyshev iteration to real-time evolution, and discuss technical aspects as computation time and implementation in detail.

I. INTRODUCTION

The dynamical mean-field theory (DMFT)[1–4] and its cluster extensions[5] are among the most successful methods to study strongly correlated electron systems in dimensions higher than one. The impurity problem within DMFT is usually solved with continuous-time quantum Monte Carlo (CTQMC) algorithms,[6–9] the numerical renormalization group (NRG)[10] or exact diagonalization (ED).[11–13] While CTQMC is computationally feasible even for problems with many bands or a high number of cluster sites, it provides numerically exact results only on the imaginary frequency axis. Many experimentally relevant frequency-dependent quantities like e.g. the conductivity therefore can only be obtained via the numerically ill-conditioned analytical continuation. NRG, by contrast, solves the problem on the real frequency axis. But it badly resolves spectral functions at high energies and cannot treat DMFT calculations with more than e.g. two bands. The limiting factor for this is the exponential growth of the *local* Hilbert space with the number of bands. Only recently, a reformulation of the mapping problem could avoid this exponential growth,[14] but it is still unclear whether this can be efficiently exploited in the context of DMFT. ED faces the problem of a limited spectral resolution due to the limited number of bath sites it can treat, although recent publications could substantially improve that.[12,13]

As the impurity problem of DMFT is one-dimensional, there has been a long-time interest to solve it using density matrix renormalization group (DMRG),[15–17] which operates on the class of matrix product states (MPS). DMRG features an unbiased energy resolution and shows no exponential growth of the local Hilbert space with respect to the number of baths. It also works directly on the real-frequency axis, avoiding analytic continuation. The earliest DMRG approach to spectral functions, the Lanczos algorithm approach,[18] is computationally cheap, but does not yield high-quality DMFT results due to its intrinsic numerical instability.[19] Recent improvements using a fully MPS-based representation of this algorithm[20] are not sufficient to resolve this issue.[21] The dynamical DMRG (DDMRG) approach[22,23] yields very precise results for single-site DMFT on the real frequency axis,[24–26] but is computationally extremely costly and therefore not competitive with other impurity solvers for DMFT.

Recently, a new approach to spectral functions based on expansions in Chebyshev polynomials[27] represented with matrix product states (CheMPS)[28–31] was introduced by two of us in Ref. 28, which gave essentially the accuracy as the DDMRG approach at a fraction of the computational cost. At the same time, the availability of real-time evolution[32–34] within time-dependent DMRG (tDMRG) and closely related methods generally also permits access to spectral functions by a Fourier transformation.[34] Both Chebyshev expansions (CheMPS)[31] and tDMRG[35] were recently seen to be applicable to the solution of the DMFT. Both approaches are computationally cheaper than DDMRG and numerically stable. For the single-impurity single-band case, results on the real-frequency axis are excellent, but for more typical present-day DMFT setups involving clusters or multiple bands, results are not available in the case of Chebyshev expansions or do so far not reach the quality of the competing QMC and NRG methods in the case of real-time evolution.

In this paper, we push the application of CheMPS to DMFT further: (i) We solve the dynamical cluster approximation (DCA)[5] for a two-site cluster and the DMFT for a two-band Hubbard model. The accuracy of the results for the latter case is better than those shown in Ref. 35, where the problem has been solved using tDMRG. (ii) We consider the experimentally relevant case of finite doping, which is significantly more complicated than the half-filled cases treated so far. (iii) We suggest a new truncation scheme for CheMPS, which allows to maintain the same error level at strongly reduced computa-

tional cost. (iv) We establish that the Chebyshev recurrence iteration can be interpreted as a discrete real-time evolution. (v) By comparing different methods to set up CheMPS, we obtain another substantial increase in computation speed. (vi) We discuss limitations of post-processing methods, which have been crucial to the success of DMRG as an DMFT impurity solver.

With these improvements, CheMPS immediately provides an efficient, precise and controlled way to solve DMFT problems with two baths (two-site clusters) on the real-frequency axis with feasible extensions to problems with more bands. The presentation proceeds as follows. After a general introduction to Chebyshev expansions of spectral functions in Sec. II, we move on to discuss its implementation in the approximate framework of MPS: in Sec. III, we present a new truncation scheme, and in Sec. IV, we discuss the mapping of the Hamiltonian to the $[-1,+1]$ convergence interval of Chebyshev polynomials, because this interacts non-trivially with efficient MPS calculations. Sec. V treats the post-processing of Chebyshev moments obtained in the expansion. These improvements are then applied to various DMFT problems. As the case of the single-impurity single-band DMFT has been treated extensively in the literature and just serves as an initial benchmark, we move those results to the Appendix. In the main text, we give examples for the relevance of our improvements to CheMPS by solving a two-site DCA in Sec. VI A and a single-site two-orbital DMFT in Sec. VI B. Technical details of these calculations are again found in the Appendix. Sec. VII concludes the paper.

II. CHEBYSHEV EXPANSION OF SPECTRAL FUNCTIONS

In this Section, we establish notation and explain the general ideas behind Chebyshev expansions of spectral functions. The zero-temperature single-particle Green's function associated with a many-body hamiltonian H is

$$G(\omega) = \langle E_0 | c \frac{1}{\omega + i0^+ - (H - E_0)} c^\dagger | E_0 \rangle, \quad (1)$$

where $c^\dagger$ creates a particle in a particular quantum state and $|E_0\rangle$ is the ground state with energy E_0. The spectral function $A(\omega) = -\frac{1}{\pi}\mathrm{Im}\, G(\omega)$ reads

$$\begin{aligned} A(\omega) &= \langle E_0 | c\, \delta(\omega - (H - E_0)) c^\dagger | E_0 \rangle \\ &= \sum_n W_n \delta(\omega - (E_n - E_0)), \end{aligned} \quad (2)$$

with weights $W_n = |\langle E_n | c^\dagger | E_0 \rangle|^2$. If evaluated exactly in a finite system, $A(\omega)$ is a comb of delta peaks, which only in the thermodynamic limit becomes a smooth function $A_{\mathrm{lim}}(\omega)$. If evaluated in an approximate way that averages over the finite-size structure of $A(\omega)$, it is possible to extract $A_{\mathrm{lim}}(\omega)$ also from a sufficiently big finite-size system. Among various techniques that provide such an approximation,[36] the most popular one is the definition of a *broadened* representation of $A(\omega)$

$$A_\eta(\omega) = \sum_n W_n h_\eta(\omega - E_n) \quad (3)$$

where the broadening function $h_\eta(\omega - E_n)$ is given by the Gaussian kernel

$$h_\eta(x) = \frac{1}{\sqrt{2\pi}\eta} e^{-\frac{x^2}{2\eta^2}}. \quad (4)$$

Besides the Gaussian kernel, a Lorentzian kernel

$$h_\eta(x) = \frac{\eta}{\pi} \frac{1}{x^2 + \eta^2} \quad (5)$$

is often implicitly used as it emerges automatically when computing the spectral function $A_\eta = -\frac{1}{\pi}\mathrm{Im}\, G(\omega + i\eta)$ from the shifted Green's function $G(\omega + i\eta)$. In general, $A_\eta(\omega)$ is indistinguishable from $A_{\mathrm{lim}}(\omega)$ if the latter has no structure on a scale smaller than η.

An efficient way to generate the broadened version $A_\eta(\omega)$ of $A(\omega)$ is via iterative expansions in orthogonal polynomials. Historically most frequently used in this context is the Lanczos algorithm, which is intrinsically numerically unstable, though. By contrast, expansions in Chebyshev polynomials can be generated in a numerically stable way. As they haven't been used much in either the DMRG or DMFT community so far, we briefly introduce them based on Ref. 27.

A. General implementation

The Chebyshev polynomials of the first kind $T_n(x)$ can be represented explicitly by

$$T_n(x) = \cos\left(n \arccos(x)\right) \quad (6)$$

or generated with the recursion

$$T_n(x) = 2xT_{n-1}(x) - T_{n-2}(x), \quad T_0 = 1, \quad T_1 = x, \quad (7)$$

which is numerically stable if $|x| \leq 1$. Chebyshev polynomials are orthonormal with respect to the weighted scalar product

$$\int_{-1}^{1} dx\, w_n(x) T_m(x) T_n(x) = \delta_{nm}, \quad (8a)$$

$$w_n(x) = \frac{2 - \delta_{n0}}{\pi\sqrt{1 - x^2}}. \quad (8b)$$

Any sufficiently well-behaved function $f(x)|_{x\in[-1,1]}$ can be expanded in Chebyshev polynomials

$$f(x) = \sum_{n=0}^{\infty} w_n(x) \mu_n T_n(x), \quad (9a)$$

$$\mu_n = \int_{-1}^{1} dx f(x) T_n(x), \quad (9b)$$

where the definition of the so-called *Chebyshev moments* μ_n via the *non-weighted* scalar product follows when applying $\int_{-1}^{1} dx\, T_m(x) \dots$ to both sides of (9a).

If $f(n)$ is smooth, the envelope of μ_n decreases at least exponentially to zero with respect to n; if $f(n)$ is the step function, the envelope decreases algebraically; and if $f(n)$ is the delta function, the envelope remains constant.[37] For a smooth function, the truncated expansion $f_N(x) = \sum_{n=0}^{N} w_n(x)\mu_n T_n(x)$ therefore approximates $f(x)$ very well if N is chosen high enough. But for the delta function, any truncated expansion yields an approximation with spurious (Gibbs) oscillations. A controlled damping scheme for the oscillations, the so-called *kernel polynomial approximation* (KPM), can be obtained with a simple modification of the Chebyshev expansion,

$$f_N^{\text{kernel}} = \sum_{n=0}^{N} w_n(x) g_n \mu_n T_n(x), \tag{10a}$$

$$g_n = \frac{(N-n+1)\cos\frac{\pi n}{N+1} + \sin\frac{\pi n}{N+1}\cot\frac{\pi}{N+1}}{N+1}, \tag{10b}$$

where g_n is the so-called Jackson kernel that leads to a very good Gaussian approximation $h_{\eta(x)}(x)$ with x-dependent width $\eta(x) = \sqrt{1-x^2}\,\pi/N$ of the delta function, and hence directly leads to (4).

In the case of the spectral function (2), one aims at an expansion of a superposition of delta functions. This can in practice often be done without damping: When expanding (2) in Chebyshev polynomials, the integration in (9b) averages over the delta-peak as well as over the finite-size peak structure of $A(\omega)$. If the weights W_n vary slowly on the scale of the spacing of finite-size peaks, the sequence μ_n approaches zero as soon as the characteristic form of this slow variation is resolved. The value of n at which this *pseudo*-convergence occurs is the one that resolves the spectral function in the thermodynamic limit $A_{\text{lim}}(\omega)$, provided that $A_{\text{lim}}(\omega)$ has no structure on a smaller scale than the spacing of finite-size peaks. Only for much higher values of n, the Chebyshev moments start deviating from zero again to then oscillate forever, resolving first the finite-size structure of $A(\omega)$ and finally the delta-peak structure. Therefore, if one can generate the sequence up to *pseudo*-convergence, then there is no need for Jackson damping.

B. Operator valued Chebyshev expansion

In order to expand the spectral function (2), one usually introduces a rescaled and shifted version of H in order to map its spectrum into the interval $[-1, 1]$, where Chebyshev polynomials are bounded and have a stable recursion relationship,

$$H' = \frac{H - E_0 + b}{a}, \quad \omega' = \frac{\omega + b}{a}. \tag{11}$$

Obviously, there is a lot of leeway in the choice of a and b, which will be found to have large implications for CheMPS (Sec. IV). Generally,

$$\begin{aligned} A(\omega) &= \frac{1}{a} A'\left(\tfrac{\omega+b}{a}\right), \text{ where} \\ A'(\omega') &= \langle t_0|\delta(\omega' - H')|t_0\rangle, \quad |t_0\rangle = c^\dagger|E_0\rangle. \end{aligned} \tag{12}$$

Expanding $A'(\omega')$ in Chebyshev polynomials yields the moments

$$\begin{aligned} \mu_n &= \int_{-1}^{1} d\omega' \langle t_0|\delta(\omega' - H')|t_0\rangle T_n(\omega') \\ &= \sum_i \int_{-1}^{1} d\omega' \langle t_0|\delta(\omega' - E_i')T_n(\omega')|E_i\rangle\langle E_i|t_0\rangle \\ &= \langle t_0|t_n\rangle, \quad |t_n\rangle = T_n(H')|t_0\rangle, \end{aligned} \tag{13}$$

Inserting the recursive definition (7) of $T_n(H')$ in the definition of $|t_n\rangle$ one obtains a practical calculation scheme for the power series expansion of $T_n(H')$

$$|t_n\rangle = 2H'|t_{n-1}\rangle - |t_{n-2}\rangle, \tag{14a}$$

$$|t_0\rangle = c^\dagger|E_0\rangle, \qquad |t_1\rangle = H'|t_0\rangle. \tag{14b}$$

One can double the expansion order with the following relation[27]

$$\bar{\mu}_{2n-1} = 2\langle t_n|t_{n-1}\rangle - \mu_1, \tag{15a}$$

$$\bar{\mu}_{2n} = 2\langle t_n|t_n\rangle - \mu_0, \tag{15b}$$

but has to be aware of the fact that moments computed this way are more prone to numerical errors.[28]

C. Retarded fermionic Green's function

In the case of fermionic problems, as encountered in DMFT, an additional technical complication comes up. The spectral representation of the fermionic retarded Green's function is the sum of its particle and hole parts

$$\begin{aligned} A(\omega) &= A^{>}(\omega) + A^{<}(-\omega), \\ A^{>}(\omega) &= \langle E_0|c_0\,\delta(\omega - (H - E_0))c_0^\dagger|E_0\rangle, \\ A^{<}(\omega) &= \langle E_0|c_0^\dagger\,\delta(\omega - (H - E_0))c_0|E_0\rangle. \end{aligned} \tag{16}$$

As $A^{\lessgtr}(\omega)$ have steps at $\omega = 0$, their representation in terms of smooth polynomials is notoriously ill-conditioned. One should therefore try to represent the smooth function $A(\omega)$ by a single Chebyshev expansion: Allowing for two different rescaling prescriptions, one has

$$A^{>}(\omega) = \frac{1}{a_1}\sum_n w_n(\omega_1'(\omega))\mu_n^{>} T_n(\omega_1'(\omega)) \tag{17a}$$

$$A^{<}(-\omega) = \frac{1}{a_2}\sum_n w_n(\omega_2'(-\omega))\mu_n^{<} T_n(\omega_2'(-\omega)) \tag{17b}$$

In order to write $A(\omega)$ in terms of a single Chebyshev expansion, one can use the symmetries $T_n(x) = (-1)^n T_n(-x)$ and $w_n(x) = w_n(-x)$. These restrict the rescaling parameters via $\omega_1'(\omega) = -\omega_2'(-\omega)$ to $a_1 = a_2 = a$ and $b_1 = -b_2$. Making the particular choice $b_1 = b_2 = b = 0$ hence defines a common expansion via[31]

$$A(\omega) = \frac{1}{a} \sum_n w_n(\tfrac{\omega}{a})(\mu_n^{>} + (-1)^n \mu_n^{<}) T_n(\tfrac{\omega}{a}). \tag{18}$$

Although $b = 0$ provides one with a controlled treatment of the step function, it comes at the price of a loss in computational speed. We will compare advantages and disadvantages of two practical shifting possibilities ($b = 0$ and $b = -a$) in detail in Sec. IV.

III. MATRIX PRODUCT IMPLEMENTATION

So far everything has been general, or it was somehow assumed that all calculations can be carried out exactly, which meets severe limitations in computational practice. Representing Chebyshev states $|t_n\rangle$ with matrix product states (MPS)[28] enables more efficient computations than in an exact representation, as the size of the effective Hilbert space can be tremendously reduced. As an MPS is usually only an approximate representation of a strongly correlated quantum state, the issue of optimal compression, i.e. the representation of a quantum state as an MPS using finite-dimensional matrices with a minimal loss of accuracy (information), is crucial. Here, we argue in the following that instead of controlling the maximal matrix dimension,[28,30,31] one should rather control the cumulated truncated weight (a proxy measure of the loss of accuracy), allowing for more efficient and more controlled calculations of Chebyshev moments.

A. Adaptive matrix dimension

If one follows through the recursive scheme for Chebyshev vectors, one starts out from a ground state, which we may assume has been obtained by a standard DMRG (MPS) calculation to extremely high precision, this means that an optimally compressed starting MPS is available where matrices have some computationally feasible dimension at very small loss of accuracy compared to the exact starting state. This, in turn, yields an extremely precise starting Chebyshev state $|t_0\rangle$. Now, in each step of the recursion (14a), one applies H' and subtracts a preceding Chebyshev state. As is well-known for MPS, the application of H' (and to a lesser extent the subtraction) lead to a drastic increase in matrix dimension, which necessitates a state compression (Sec. 4.5 of Ref. 17) of the new Chebyshev state $|\widetilde{t_n}\rangle$ to a computationally manageable state $|t_n\rangle$ with smaller matrix dimension m, which generates the error δ

$$\begin{aligned} \mu_n &= \langle t_0|\widetilde{t_n}\rangle = \langle t_0|t_n\rangle \pm \delta, \\ |\widetilde{t_n}\rangle &= 2H'|t_{n-1}\rangle - |t_{n-2}\rangle, \\ \delta^2 &= \left|\langle t_0|(|\widetilde{t_n}\rangle - |t_n\rangle)\right|^2 \\ &< ||t_0\rangle|^2 \left||\widetilde{t_n}\rangle - |t_n\rangle\right|^2 < ||t_0\rangle|^2 \varepsilon_{\text{compr}}(m). \end{aligned} \tag{19}$$

Here, we used the upper error bound[38] provided by the cumulated truncated weight $\varepsilon_{\text{compr}}(m)$

$$\left||\widetilde{t_n}\rangle - |t_n\rangle\right|^2 \leq \varepsilon_{\text{compr}}(m) = \sum_{i=1}^{L-1} \epsilon_i(m), \tag{20}$$

where $\epsilon_i(m)$ is the sum over the discarded reduced density-matrix eigenvalues per bond and the sum over i is over all bonds. This error bound for a single step of the recursion unfortunately does *not* provide a statement about the total error that accumulates over all compression steps in preceding Chebyshev recursion steps. Still, we experienced that the numerical stability of the Chebyshev recursion rather leads to a helpful compensation of errors of single recursion steps. Fig. 1 shows that the *total* error stays at the order of the error of a *single* step $||t_0\rangle|^2 \varepsilon(m)$ also for high iteration numbers n. In the case in which one fixes the matrix dimension m, Fig. 1 shows a steady, uncontrolled increase of the total error. This is particularly undesirable in view of the desired post-processing of Chebyshev moments (Sec. V).

Another possibility would be to fix the local discarded weight $\epsilon_i(m)$ as defined in (20). But this does in general *not* lead to a viable computation scheme for impurity models: In the simplest and most-employed chain representation of impurity models, the impurity site is located at an edge of the chain. Fixing the same value for $\epsilon_i(m)$ for all bonds then leads to extremely high matrix dimensions in the center of the chain, i.e. in the center of the bath, where entanglement for systems with open boundary conditions is maximal. The relevant entanglement, by contrast, is the one between the impurity site and the bath. This becomes clear when noticing that upon projecting the Chebyshev state $|t_n\rangle$ on $|t_0\rangle$ to compute μ_n, only correlations with respect to the *local* excitation $c^\dagger|E_0\rangle$ are measured. The high computational effort of high matrix dimensions that follows when faithfully representing entanglement *within* the bath, is therefore in vain. For geometries with the impurity at the center, like the two-chain geometry used for the two-bath problems in this paper, the preceding argument is not valid. An inhomogeneous distribution of matrix dimensions with high values at the center and low values at the boundaries is *a priori* consistent with open boundary conditions. This distribution can therefore be achieved by fixing a constant value for $\epsilon_i(m)$ for each bond. Another possible truncation scheme could be obtained by using an estimator for the correlations of the impurity with the bath, which then fixes the matrix dimensions as a function of bonds $m(i)$ (distance to the impurity). Both approaches

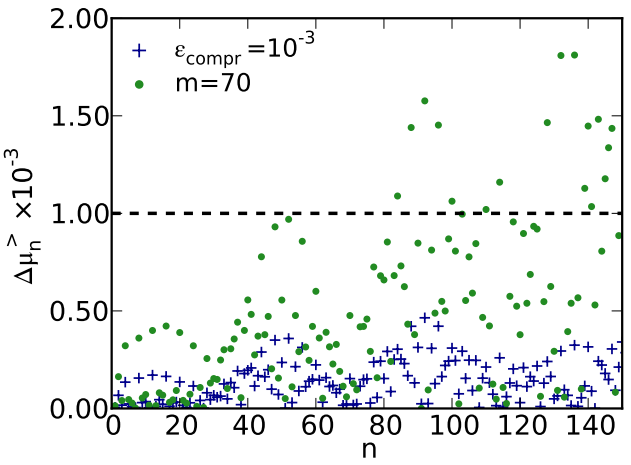

FIG. 1. (Color online) Error of Chebyshev moments $\mu_n^>$ (as they appear in (17a)), computed as $\Delta\mu_n^> = |\mu_n^> - \tilde{\mu}_n^>|$, where $\tilde{\mu}_n^>$ is obtained with a quasi-exact calculation with high matrix dimension $m = 200$. If one fixes the matrix dimension m, the error steadily increases. If, instead, one fixes the cumulated truncated weight $\varepsilon_{\text{compr}}$, the error remains approximately constant and does not accumulate. This is the procedure followed in this paper. As here, $||t_0\rangle|^2 = 1$, $\varepsilon_{\text{compr}}$ equals the upper error bound of a single compression step. Results shown are for the spectral function of the half-filled single-impurity Anderson model (SIAM) (Appendix C 1) with semi-elliptic density of states of half-bandwidth D, interaction $U = 2D$, represented on a chain with $L = 40$ lattice sites. This is equivalent to considering the local density of states at the first site of a fermionic chain with constant hopping $t = D/2$ and an interaction of $U = 4t$ that acts solely at the first site.

constitute possible future refinements. For simplicity, in this paper, we consider the truncation scheme that fixes a constant value of m based on the cumulative truncated weight.

B. State compression

During the repeated solution of (14a) we monitor the truncated weight $\varepsilon_{\text{compr}}$. If $\varepsilon_{\text{compr}}$ exceeds a certain threshold of the order of 10^{-4} to 10^{-3}, we slightly increase the matrix dimension m, and repeat the compression. For the first compression step we take as an initial guess the previous Chebyshev state $|t_{n-1}\rangle$. For repeated compression steps we take as an initial guess the state of the previous compression step. It turns out that in practice one almost never faces repeated compressions, which gains one approximately a factor 2 in computation speed compared to the error monitoring of Ref. 28: in Ref. 28, the authors keep the matrix dimension fixed and variationally[17] compress an exact representation of the right hand side of (14a) for fixed m by repeated iterations ("sweeps") until the error

$$\left| 1 - \frac{\langle t'_n | t_n \rangle}{|| \, |t'_n\rangle \, || \; || \, |t_n\rangle \, ||} \right|, \tag{21}$$

drops below a certain threshold. Here, $|t'_n\rangle$ denotes the state before a sweep, and $|t_n\rangle$ the state after a sweep. This error measure is not related to the factual error of Chebyshev moments, for any but the first sweep. Its monitoring is costly to compute and leads to at least two compression sweeps.

IV. OPTIMAL CHEBYSHEV SETUP

One can generally state that the effectiveness of the MPS evaluation of the Chebyshev recursion (14a) for a certain system is unknown *a priori* but must be experienced by observing how strong entanglement in the Chebyshev vectors, and therefore matrix dimension m needed for a faithful representation grows as compared to the speed of convergence of μ_n. For very high iteration numbers one will always reach a regime in which matrix dimensions have grown so much that further calculations become too expensive computationally. This is known from tDMRG as *hitting an exponential wall* and defines an *accessible time scale*, or in our case, an accessible expansion order. In the case of the computation of Chebyshev moments, the accessible time scale strongly depends on the choice of the shifting parameter b, which leads us to consider the two cases $b = 0$ and $b = -a$.

Comparing these cases, one finds a much slower speed of convergence of the Chebyshev moments in the case $b = 0$ than in the case $b = -a$. Putting that differently: per fixed amount of entanglement growth (application of H in one step of (14a)), much less information about the spectral function is extracted in case $b = 0$ than in case $b = -a$. Independent of that, one finds that the advantage of the choice $b = 0$ to provide one with an analytic expression for $A(\omega)$ in terms of a single Chebyshev expansion (Sec. II C) can be detrimental. We therefore need to study both cases in more detail.

A. No shift: $b = 0$

If choosing $b = 0$, one can derive a scaling property of Chebyshev moments that simplifies extracting the thermodynamic limit as well as the examination of computational performance.

The spectral function of a one-particle operator $A(\omega)$ is non-zero only in the vicinity of the groundstate energy $\omega = 0$, up to a distance of the order of the single-particle bandwidth W_{single}. The rescaled spectral function $A'(\omega')$ is non-zero up to a distance of W_{single}/a from $\omega' = 0$. For all rescaling parameters a that have been proposed up to now,[27,28,31] one has $W_{\text{single}}/a < \frac{1}{2}$. Usually W_{single}/a is much smaller than the upper bound $\frac{1}{2}$.

As $\arccos(x) = \pi/2 - x - x^3/6 + \ldots$ is well approximated by its linear term already for $|x| < 0.5$, Chebyshev polynomials (6) behave like a shifted cosine function in the region where $A'(\omega')$ is non-zero. The expansion of $A'(\omega')$ in Chebyshev polynomials is therefore essentially equivalent to a Fourier expansion. This means that the iteration number n of the Chebyshev expansion has the same meaning as a discrete propagation time, the evolution of which is mediated by simple applications of H instead of the ordinary continuous time propagation e^{-iHt}. To answer the question of whether an ordinary time evolution[35] is more effective in generating information about the spectral function, one has to study the entanglement entropy production of repeated applications of H compared to the one of e^{-iHt}. The following results are first steps in this direction.

In discrete time evolution, the rescaling of the frequency directly translates to an inverse scaling of time. Considering two calculations of Chebyshev moments, one for $\mu_n^{(1)}$ performed with H' and another for $\mu_n^{(a)}$ performed with H'/a, one therefore has the simple approximate relation

$$\begin{aligned}\mu_n^{(1)} &\sim \langle t_0| \cos(nH')|t_0\rangle \\ &= \langle t_0| \cos(anH'/a)|t_0\rangle \sim \mu_{na}^{(a)}. \end{aligned} \tag{22}$$

This means that if rescaling with a, one has to compute a times more Chebyshev moments than in the case without rescaling. An exact version of statement (22) is given in (A2) in Appendix A. Fig. 2(a) illustrates the scaling property (22) for a system of fixed size.

a. Extracting the thermodynamic limit. One direct application of the scaling property (22), lies in the study of the thermodynamic limit by comparing systems of increasing size L. For low values of n, even small systems have the same Chebyshev moments as in the thermodynamic limit. Finite-size features are averaged out in the integral (9b) as long as $T_n(x)$ oscillates slowly enough. $T_n(x)$ oscillates n times on $[-1, 1]$. An Nth order Chebyshev expansion therefore resolves features on the scale $2/N$, which on the original energy scale is $2a/N$. Finite-size oscillations appear at a spacing of W_{single}/L, where W_{single} is the single-particle bandwidth. Equating resolution with the spacing of finite-size oscillations

$$2a/N_{\text{finsize}} = W_{\text{single}}/L, \tag{23}$$

gives the expansion order N_{finsize} at which finite-size features are first resolved. Fig. 2(b) illustrates these statements by comparing Chebyshev moments computed for different system sizes.

b. Optimizing computation time. Fig. 3 shows how computation time depends on the rescaling constant a for the example of the moments shown in Fig. 2(a). As already qualitatively stated previously[28,31], one observes that upon using a lower value of a computation time is reduced. In all cases, computation time diverges exponentially (Fig. 2(b)). Note that rescaling with a higher value of a allows to compute at smaller matrix dimensions. Note further that if choosing a too small, numerical errors can render the recursion (14a) unstable. In contrast to common belief, it is possible to use much smaller values of a than the full many-body bandwidth. Achieving even smaller values of a can be done with the so-called *energy truncation*[28], but after several tests, we did not find this to lead to an effective speed-up of calculations. We therefore discard it in our calculations as

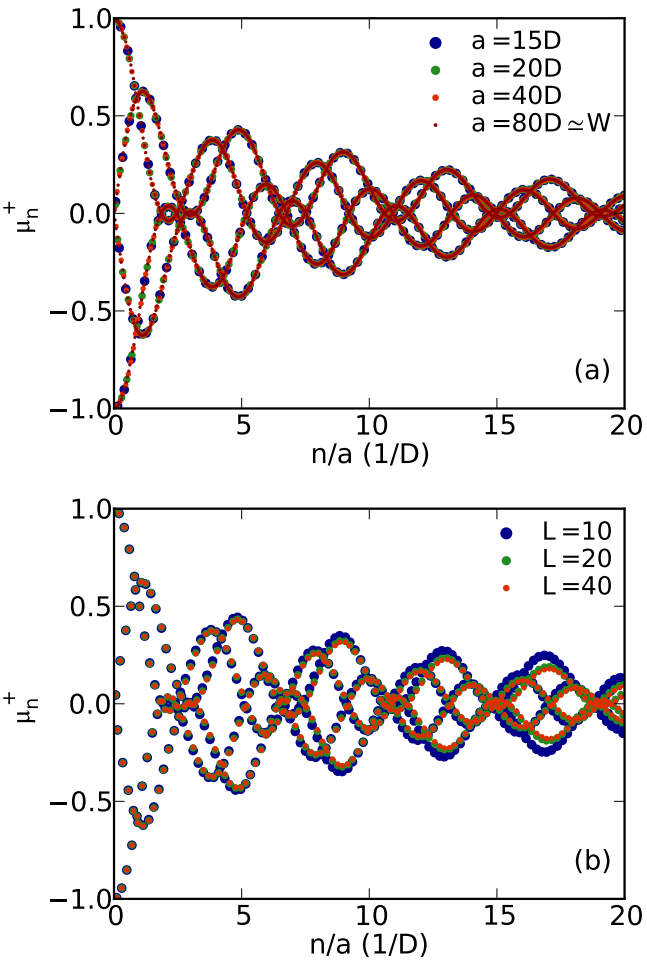

FIG. 2. (Color online) Panel (a): Chebyshev moments $\mu_n^>$ vs n/a for fixed system size and different values of a and $b = 0$. Except for a different total number of points, the rescaled moments all lie on the line obtained when $a \to \infty$ and n/a becomes continuous. Here, we study the half-filled SIAM (Appendix C 1) with semi-elliptic density of states of half-bandwidth D and $U = 2D$, represented on a chain with length $L = 80$. The full many-body bandwidth is $W \simeq 80D$. Panel (b): Chebyshev moments for different system sizes L. Except for the system size and the scaling parameter, parameters are the same as in panel (a). Here all calculations were done with a rescaling constant of $a = 20D$. For low values of n, the results for different system sizes are virtually indistinguishable. For higher values of n, moments start to disagree as finite-size features start to be resolved. The $L = 80$ and the $L = 40$ results would be indistinguishable in this plot.

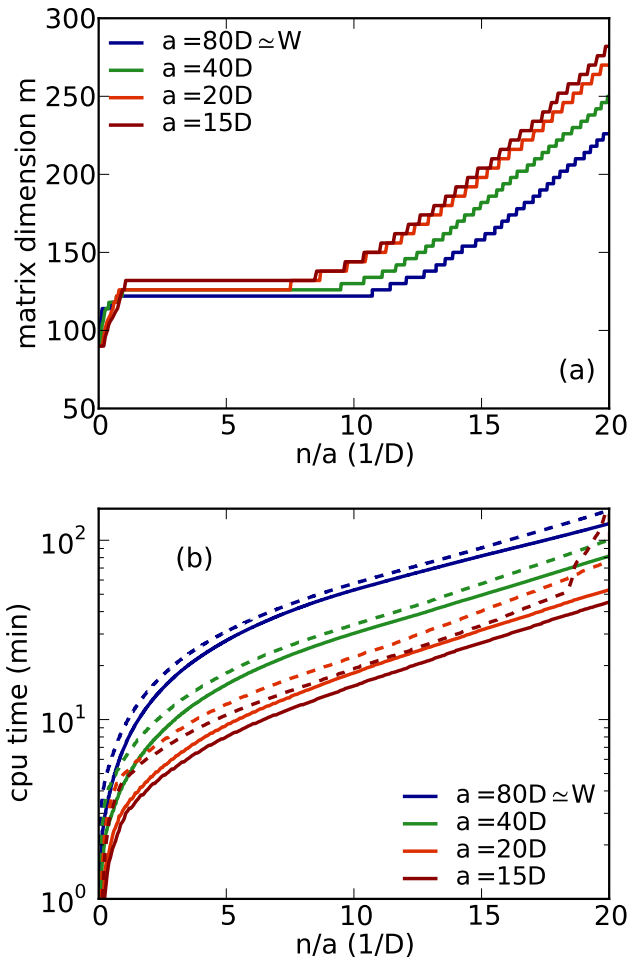

FIG. 3. (Color online) Performance of the adaptive matrix dimension algorithm (Sec. III A) for the example described in the caption of Fig. 2. Panel (a): Adaption of matrix dimensions for different rescaling factors, fixing a truncation error of $\varepsilon_{\text{compr}} = 10^{-3}$. Panel (b): Computer time needed to generate the same amount of information for different scalings running on a single-core 2.0 GHz workstation. Solid lines: fixing a truncation error of $\varepsilon_{\text{compr}} = 10^{-3}$. Dashed lines: $\varepsilon_{\text{compr}} = 5 \times 10^{-4}$. The iteration number where the irregular behavior of the dashed line for $a = 15D$ starts corresponds to the point where numerical errors render the Chebyshev recursion unstable. Note that while small a leads to the largest matrix sizes, which is costly in MPS, the overall cost of CPU time nevertheless is lowest, as a smaller expansion order is needed.

a source of additional tuning parameters. We have also tested the idea of Ganahl *et al.*[31] to map the spectrum of H into $[-1, 1]$ via $1 - \exp(\beta H)$. The idea might be worth to study in more detail, but again, we could not gain any performance improvement over a simple rescaling procedure.

B. Shifting by $b = -a$.

The choice $b = -a$ in (11) makes an analytic expression of the complete spectral function $A(\omega) = A^+(\omega) + A^-(-\omega)$ in terms of a single Chebyshev expansion impossible, but has beneficial effects on the computation time. This is to be understood in the following sense: Due to the increased oscillation frequency of $T_n(x)$ close to the interval boundaries of $[-1, 1]$, the integral (9a) extracts much more information about the spectral function in the vicinity of these boundaries. This is reflected e.g. in the fact that the width of the Gaussian obtained by the kernel polynomial expansion approaches zero close the interval boundaries of $[-1, 1]$ (see the discussion below (10b)). It is therefore desirable to shift the relevant part of the spectral function, the part slightly above the Fermi edge, to match the left boundary -1. This is achieved by the choice $b = -a$. In practice, one adds a small correction $a\epsilon$, $\epsilon \sim 10^{-3}$, to avoid problems with the diverging weight function $w_n(x)$ in (8b).

Another advantage of the $b = -a$ setup is that one can use a smaller scaling constant a than in the $b = 0$ setup. The Chebyshev iteration becomes unstable when the iteration number n becomes so high that $|t_n\rangle$ has accumulated erroneous contributions from eigen states with eigen energies $E'_n = (E_n - E_0 + b)/a > 1$. For fixed a, the additional subtraction in the $b = -a$ setup ensures that the instability appears for a higher iteration number than in the $b = 0$ setup. Therefore, the $b = -a$ setup allows smaller values of a. We finally note that the choice $b = -a$ is equivalent to the choice suggested by Weiße *et al.*[27], if one rescales with the full many-body bandwidth $a = W$. In this case, the computation can be carried out to arbitrarily high order and will never become unstable. In the $b = 0$ setup, one would have to choose $a = 2W$ to reach arbitrarily high expansion orders.

In Fig. 4(a), we plot Chebyshev moments for both types of shifts $b = 0$ and $b = -a$. The moments obtained for $b = 0$ show a slow structureless oscillation whereas the moments obtained for $b = -a$ show a much faster oscillation. Fig. 4(b) shows that upon using the same rescaling constant a and the same expansion order $N = 100$, which leads to very similar entanglement growth, both shift types differ strongly in the achieved resolution. To resolve at least the right Hubbard peak with a $b = 0$ calculation at the resolution of $b = -a$ calculation, one needs $N = 300$ moments. As computation time increases exponentially (Fig. 3(b)) with respect to expansion order N in both cases, this difference is highly relevant.

We apply both setups, $b = 0$ and $b = -a$, to the benchmark test of the DCA in Sec. VI A, and find a significant speed-up for $b = -a$ at a small loss in accuracy. Previously,[31] only $b = 0$ has been considered for the solution of the DMFT.

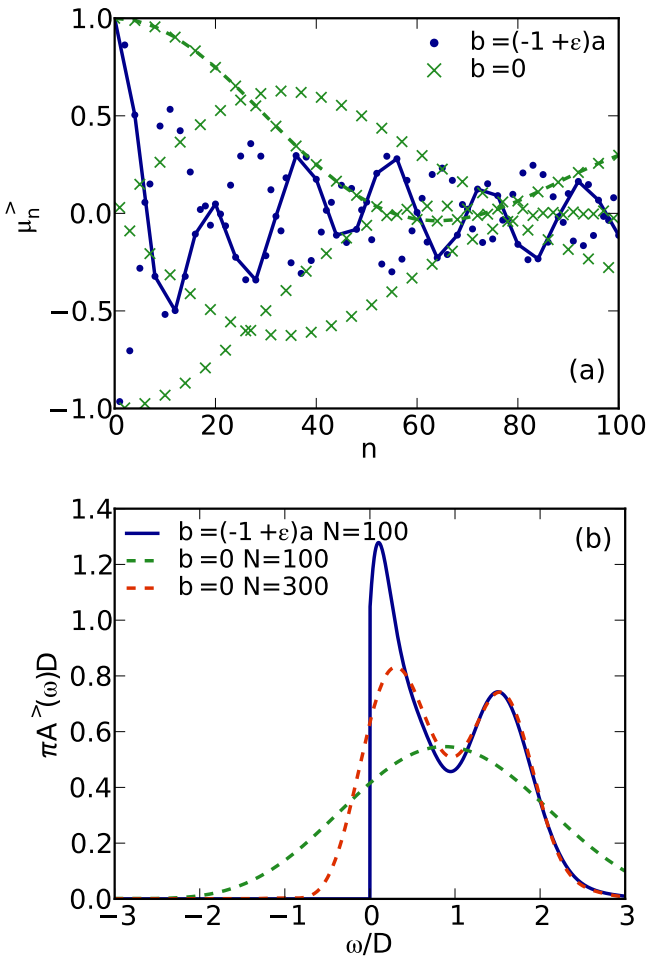

FIG. 4. (Color online) Local particle density of states of the half-filled SIAM (Appendix C 1) with semi-elliptic density of states of half-bandwidth D. $L = 40$, $U = 2D$ and $a = 30D$ in all cases. Panel (a): Chebyshev moments. Lines connect every 4th moment and by that reveal the relevant slow oscillation. They are a guide to the eye. Panel (b): Corresponding spectral functions evaluated using Jackson damping (10b). The $b = 0$ calculation requires three times more iterations than the $b = -a$ calculation to resolve the right Hubbard peak with the same resolution. In this case the central peak is still much better resolved for $b = -a$.

V. POST-PROCESSING MOMENTS

Whereas Jackson damping (10b) can be seen as one possibility to post-process Chebyshev moments in order to achieve uniform convergence even for the truncated Chebyshev expansion of a delta function, there is another, fundamentally different approach.

The computation of the Chebyshev moments becomes very costly for high iteration numbers. In the case in which Chebyshev moments start to follow a regular pattern when n exceeds a certain threshold, it is possible to continue this pattern to infinity, and one can avoid the costly computation of moments. Consider the typical example in which the spectral function is a superposition of Lorentzians (quasiparticle peaks) and of a slowly varying background density. As for low values of n, $T_n(x)$ extracts information via (9b) only about the slowly varying background density, while for high values of n, $T_n(x)$ extracts information only about the sharp and regular Lorentzian structures, μ_n starts to follow a regular pattern for high numbers of n. For a sum of Lorentzians, with weights α_i, widths η_i, and positions ω_i, this pattern can be obtained analytically:

$$A_{\mathrm{Lor}}(\omega) = \sum_i \alpha_i \frac{\eta_i}{\pi} \frac{1}{(\omega-\omega_i)^2+\eta_i^2},$$
$$\Rightarrow \quad \mu_n \simeq \sum_i \alpha_i \cos(n(\omega_i - \frac{\pi}{2}))e^{-n\eta_i}, \qquad (24)$$

as shown in Appendix B. If one recalls (Sec. IV) that the Chebyshev recursion corresponds to a discrete time evolution if choosing $b = 0$, the result of (24) could have been anticipated.

Fig. 5(a) shows the spectral density for a SIAM together with a fitted superposition of three Lorentzians. Their difference corresponds to a background density that is composed of either slowly varying features or features with negligible weight. Fig. 5(b) shows the corresponding Chebyshev moments. The slowly varying background density only contributes for the first 200 moments. After that, the Chebyshev moments for the superposition of Lorentzians starts to be a very good approximation to the original moments, and it seems unnecessary to compute more than about 400 moments. For $200 < n < 400$, one can simply fit the analytical expression (24) to the original data. Using the analytical expression with the fitted parameters, one can then continue the Chebyshev moments to infinity.

Fitting (24) to the data between iterations 200 and 400 is a nonlinear optimization problem, which can easily be solved numerically. Still, there exists a linear reformulation of this optimization problem, coined under the name *linear prediction*[40]. The linear problem can be analytically reformulated as a matrix inversion problem. Its solution is faster and more stable than that of the original non-linear problem. This allows in principle to optimize a superposition of many more Lorentzians than in the non-linear case.

1. *Linear prediction*

In the context of time evolution *linear prediction* has been long established in the DMRG community,[41,42] but it has only recently been applied to the computation of Chebyshev moments.[31] The optimization problem for the sequence μ_n becomes linear, if the sequence can be defined *recursively*

$$\tilde{\mu}_n = -\sum_{i=1}^{p} a_i \mu_{n-i}, \qquad (25)$$

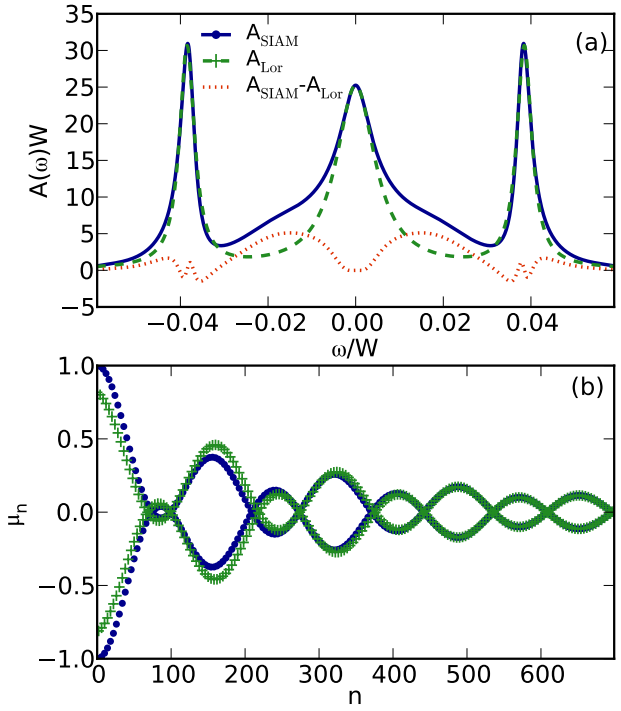

FIG. 5. (Color online) Panel (a): $A_{\mathrm{SIAM}}(\omega)$ for a semi-elliptic density of states, half filling and $U = 2D$ (Appendix C 1). Quantities are shown in units of the full many-body bandwidth W. The superposition of three Lorentz peaks $A_{\mathrm{Lor}}(\omega)$ has been fitted to $A_{\mathrm{SIAM}}(\omega)$. Panel (b): Corresponding Chebyshev moments. The result presented here was obtained with a $L = 40$ fermionic chain and CheMPS. It agrees with the result of Raas *et al.*[39], see Appendix C 1. The legend in panel (a) is valid also for panel (b).

which is easily found to be equivalent to (24)[42]. The strategy is then as follows. Compute $n = N_c$ Chebyshev moments, and predict moments for higher values of n using (25). The coefficients a_i are optimized by minimizing the least-square error $\sum_{n\in\mathcal{N}_{\mathrm{fit}}} |\tilde{\mu}_n - \mu_n|^2$ for a subset $\mathcal{N}_{\mathrm{fit}} = \{N_c - n_{\mathrm{fit}}, \ldots, N_c - 1, N_c\}$ of the computed data. We confirmed $n_{\mathrm{fit}} = N_c/2$ to be a robust choice,[31,42] small enough to go beyond spurious short-time behavior and large enough to have a good statistics for the fit. Minimization yields

$$R\boldsymbol{a} = -\boldsymbol{r}, \quad \boldsymbol{a} = -R^{-1}\boldsymbol{r}, \tag{26}$$
$$R_{ji} = \sum_{n\in\mathcal{N}_{\mathrm{fit}}} \mu^*_{n-j}\mu_{n-i}, \quad r_j = \sum_{n\in\mathcal{N}_{\mathrm{fit}}} \mu^*_{n-j}\mu_n.$$

We found that linear prediction loses its favorable filter properties if choosing p to be very high. Therefore one should restrict the number of Lorentzians to $p = \min(n_{\mathrm{fit}}/2, 100)$. Furthermore, one adds a small constant $\delta = 10^{-6}$ to the diagonal of R in order to enable the inversion of the singular matrix R. Defining[42]

$$M = \begin{pmatrix} -a_1 & -a_2 & -a_3 & \ldots & -a_p \\ 1 & 0 & 0 & \ldots & 0 \\ 0 & 1 & 0 & \ldots & 0 \\ \vdots & \ddots & \ddots & \ddots & \vdots \\ 0 & 0 & \ldots & 1 & 0 \end{pmatrix},$$

one obtains the predicted moments $\tilde{\mu}_{N_c+n} = (M^n \boldsymbol{\mu}_{N_c})$, where $\boldsymbol{\mu}_{N_c} = (\mu_{N_c-1}\ \mu_{N_c-2}\ \ldots\ \mu_{N_c-p})^T$. The matrix M usually has eigenvalues with absolute value larger than 1, either due to numerical inaccuracies or due to the fact that linear prediction cannot be applied as μ_n rather increases than decreases on the training subset $\mathcal{N}_{\mathrm{fit}}$. In order to obtain a convergent prediction, we set the weights that correspond to these eigenvalues to zero measuring the ratio of the associated discarded weight compared to the total weight. If this ratio is higher than a few percent, we conclude that linear prediction cannot yet be applied and restart the Chebyshev calculation to increase the number of computed moments N_c.

2. *Failure of linear prediction*

It is not *a priori* clear that the spectral function can be well approximated by a superposition of Lorentzians, although this is true for the SIAM as shown in Fig. 5. Other types of smooth functions lead to a different functional dependence of the moments on n than the exponentially damped behavior. Close to phase transitions, e.g. one might find an algebraic decay in the time evolution, corresponding to an algebraic decay in the Chebyshev moments. If the spectral function has rather Gaussian shaped peaks, the decrease of Chebyshev moments is $\propto e^{-(\sigma n)^2}$ (Appendix B). For both scenarios, linear prediction is a non-controlled extrapolation scheme. It still extracts oscillation frequencies (peak positions) with high reliability, but predicts a wrong decrease of the envelope, which often leads to an overestimation of peak weights.

In practice it turns out that a combination of *damping* with a Jackson kernel (Kernel Polynomial Method) and *linear prediction* is a powerful way to get controlled estimates for the spectral function. While damping always underestimates peak heights, linear prediction typically overestimates peak heights. Both methods trivially converge to the exact result, when $N_c \to \infty$. One therefore obtains upper and lower bounds for the spectral function. This is particularly valuable in the DMFT as overestimated (diverging) peak heights can spoil convergence of the DMFT loop.

A historically much used alternative to linear prediction, suitable for arbitrary forms of the spectral function, is an extrapolation of Chebyshev moments using maximum entropy methods[43]. These suffer from severe numerical instabilities, though. Of course, one might also

think of fitting another ansatz than the one of the exponential decrease. As it is *a priori* not clear which ansatz should be better, it is meaningful to stick to the easily implemented linear prediction that is moreover known to be applicable for the description of quasi-particle features.

VI. RESULTS FOR DMFT CALCULATIONS WITH TWO BATHS

A. Results for two-site DCA (VBDMFT)

In order to benchmark the Chebyshev technique for a two-bath situation, which goes beyond previous work[31] (see Appendix C), we study the Hubbard model on the two dimensional square lattice

$$H_{\mathrm{Hub}} = \sum_{\boldsymbol{k}\sigma} \varepsilon_{\boldsymbol{k}} c^\dagger_{\boldsymbol{k},\sigma} c_{\boldsymbol{k},\sigma} + U \sum_i n_{i\uparrow} n_{i\downarrow}, \tag{27}$$
$$\varepsilon_{\boldsymbol{k}} = -2t(\cos(\boldsymbol{k}_x) + \cos(\boldsymbol{k}_y)) - 4t' \cos(\boldsymbol{k}_x)\cos(\boldsymbol{k}_y).$$

in a two-site dynamical cluster approximation[5] (DCA) developed by Ferrero *et al.*[44]. This so-called *valence bond* DMFT (VBDMFT) is a minimal description of the normal phase of the high-temperature superconductors, using a minimal two patches DCA cluster. It leads to a simple physical picture of the pseudogap phase in terms of a selective Mott transition in the momentum space. We choose this model here as a benchmark since its solution contains low energy features in the spectral functions (pseudogap), which have required high-precision QMC computations followed by a careful Padé analytic continuation. Moreover, real-frequency computations are very important for the comparison with experiments that measure e.g. the optical conductivity along c-axis.[45] It is therefore a non-trivial case where DMRG impurity solvers would bring significant improvements over the QMC in practice.

To set up the VBDMFT, one splits the Brioullin zone into a *central* patch $P_+ = \{\boldsymbol{k} \,|\, |k_x| < k_0 \wedge |k_y| < k_0\}$, where $k_0 = \pi(1 - 1/\sqrt{2})$, and a *border* patch $P_- = \{\boldsymbol{k} \,|\boldsymbol{k} \notin P_+\}$. In the DCA, the $\boldsymbol{k}$-dependence of the self-energy $\Sigma_\kappa(\omega)$ within each patch is neglected and one computes a Green's function for a patch by averaging over all $\boldsymbol{k}$ vectors in the patch

$$G_\kappa(\omega) = \frac{1}{|P_\kappa|} \sum_{\boldsymbol{k}\in P_\kappa} \frac{1}{\omega + \mu - \varepsilon_{\boldsymbol{k}} - \Sigma_\kappa(\omega)}, \tag{28a}$$
$$\Sigma_\kappa(\omega) = G_{0\kappa}(\omega)^{-1} - G_\kappa(\omega)^{-1}. \tag{28b}$$

Representing the non-interacting baths in a chain-geometry, and taking the two impurities to be the first of two chains $c_{\kappa\sigma} \equiv c_{0\kappa\sigma}$, the model Hamiltonian that needs to be solved is

$$\begin{aligned} H &= H_d + H_{b,+} + H_{b,-} \\ H_d &= \sum_{\substack{\kappa=\pm \\ \sigma=\uparrow,\downarrow}} \left(\bar{t}_\kappa + \varepsilon_0\right) n_{\kappa\sigma} + \frac{U}{2} \sum_{\substack{\kappa=\pm \\ \overline{\kappa}=-\kappa}} \big(n_{\kappa\uparrow} n_{\kappa\downarrow} + n_{\kappa\uparrow} n_{\overline{\kappa}\downarrow} \\ &\quad + c^\dagger_{\kappa\uparrow} c^\dagger_{\kappa\downarrow} c_{\overline{\kappa}\downarrow} c_{\overline{\kappa}\uparrow} + c^\dagger_{\kappa\uparrow} c^\dagger_{\overline{\kappa}\downarrow} c_{\kappa\downarrow} c_{\overline{\kappa}\uparrow}\big), \\ H_{b,\kappa} &= \sum_{i=0,\sigma}^{L_\kappa} t_{i\kappa} (c^\dagger_{i\kappa\sigma} c_{i+1,\kappa\sigma} + \text{h.c.}) + \sum_{i=1,\sigma}^{L_\kappa} \varepsilon_{i\kappa} n_{i\kappa\sigma}, \end{aligned} \tag{29}$$

where $\varepsilon_0 = -\mu$ and the term $\bar{t}_\kappa = \frac{1}{|P_\kappa|} \sum_{k\in P_\kappa} \varepsilon_k$ accounts for high-frequency contributions of the hybridization function (see Appendix D 4).

The κ-space interaction term in (29) arises when diagonalizing the hybridization function of a real-space two-site cluster $c_{\pm\sigma} = \frac{1}{\sqrt{2}}(c_{1\sigma} \pm c_{2\sigma})$, where $c_{1\sigma}, c_{2\sigma}$ are annihilation operators for the cluster sites in real-space, and $c_{\pm\sigma}$ for the cluster sites in κ space. In real-space, the interaction is a simple Hubbard expression, but then the hybridization function is non-diagonal. A diagonal hybridization function, which leads to two uncoupled baths for the patches and by that allows a simple chain-geometry for the whole system, is therefore only possible in κ-space. The more complex form of the interaction in κ-space does not affect the efficiency of DMRG.

We iteratively solve the self-consistency equation obtained by inserting the self-energy estimates of the impurity model (29) into the lattice Green functions (28a). We do that on the real-energy axis with an unbiased energy resolution. The details of this calculation are described in Appendix D.

In Fig. 6(a) and (b), we compare our CheMPS results for the spectral densities of the two momentum patches with those of Ferrero *et al.*[44] obtained using CTQMC and analytical continuation. We observe a good overall agreement between the two methods, in particular at low frequencies. Low energy features (pseudogap), in particular in $A_-(\omega)$, are well reproduced by both methods. At high energy (Hubbard bands) however, there are some differences between QMC and CheMPS (and also between the two variants of CheMPS). This is to be expected since the Padé analytic continuation technique used on the QMC data in Ref. 44 is not a precision method at high energy.

In Fig. 6(c) and (d), we do the analogous comparison on the imaginary axis, and find much better agreement. On the imaginary axis, the QMC results can be considered numerically exact. The very low temperature ($\beta D = 200$) used for QMC should yield results that are indistinguishable from a zero-temperature calculation. The slight disagreement of our data and the QMC data on the Matsubara axis could probably be removed if we were able to reach higher expansion orders. One DMFT iteration for the presented $b = 0$ calculation took around 5 h running on four cores with 2.5 GHz. Convergence is achieved after 10 iterations starting from the

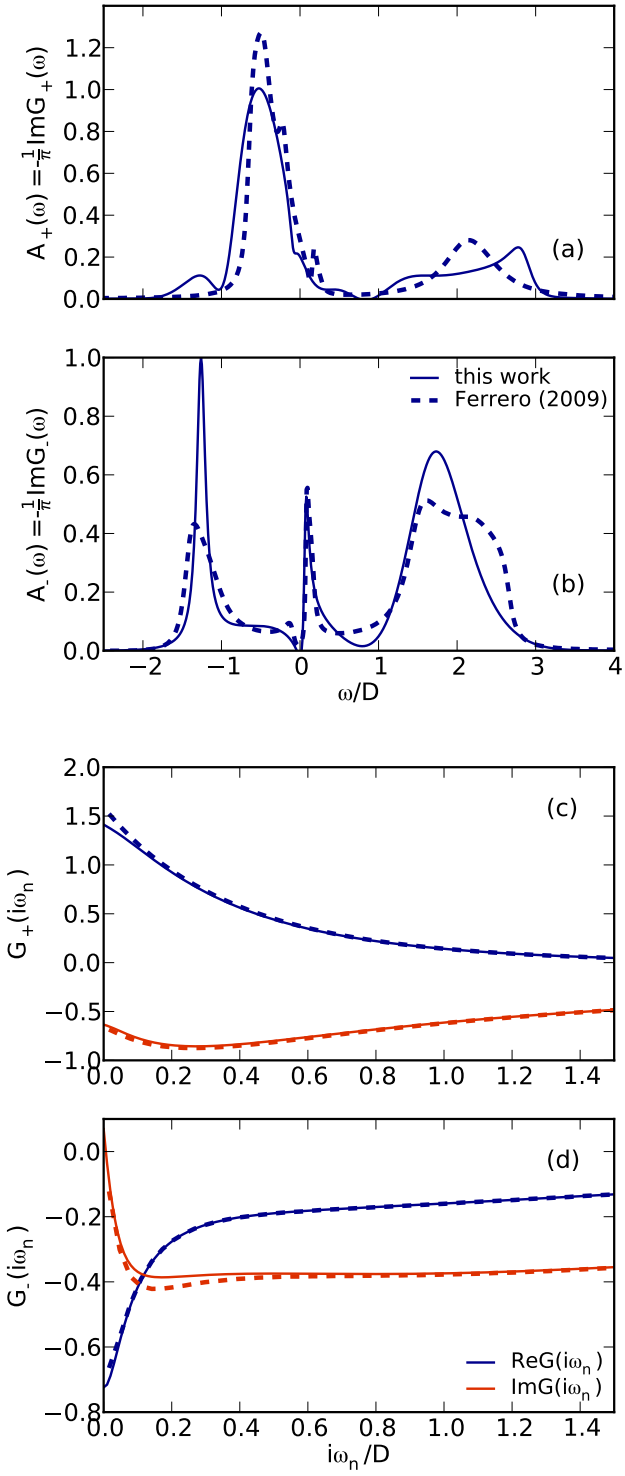

FIG. 6. (Color online) Spectral functions (a,b) and Green's functions on the imaginary axis (c,d) within VBDMFT[44] for $U = 2.5D$ and $n = 0.96$. We compare our zero-temperature CheMPS results (solid lines) with CTQMC data for $T = 1/200$ (dashed lines) from Ferrero *et al.*[44]. For this computation, we used the $b = 0$ setup, a chain length of $L = 30$ per bath, a truncation error of $\varepsilon_{\mathrm{compr}} = 10^{-3}$, and $N/a = 60/D$, $a = 40D$.

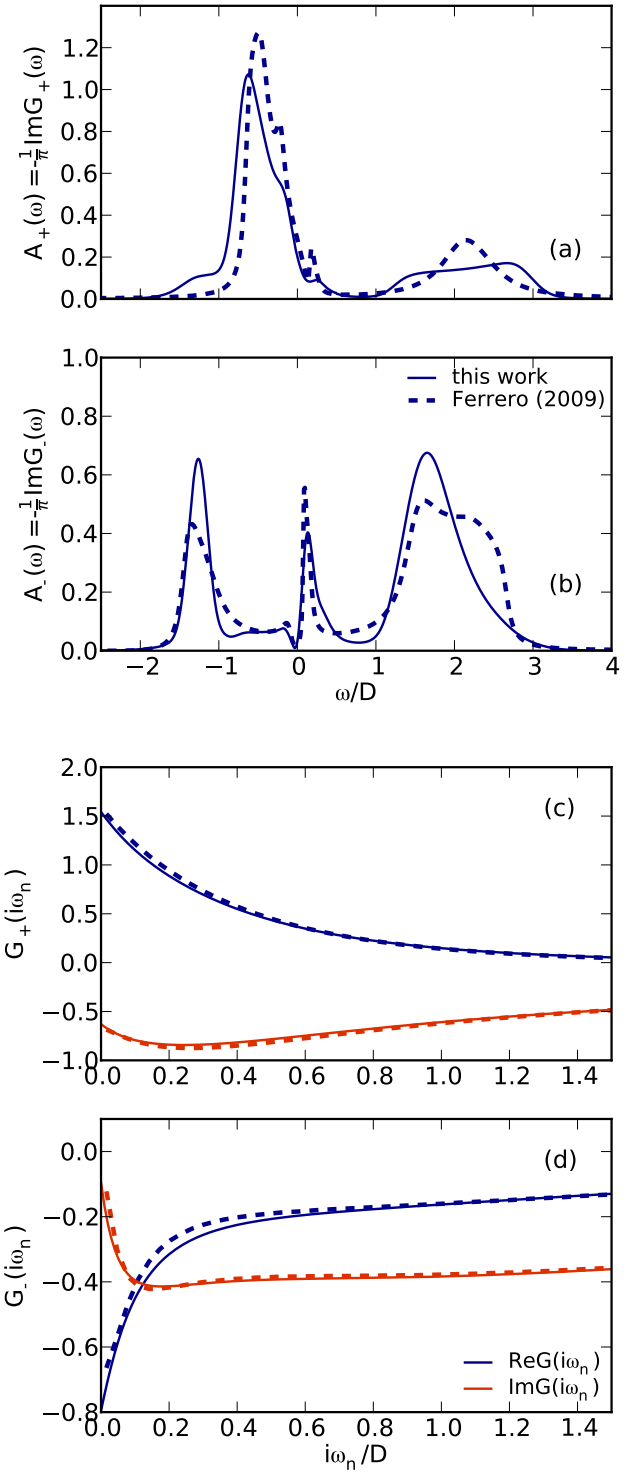

FIG. 7. (Color online) The same comparison as in Fig. 6. For this computation, we used the $b = -a$ setup, a chain length of $L = 40$ per bath, a truncation error of $\varepsilon_{\mathrm{compr}} = 10^{-3}$, and $N = 450$ and $a = 15D$. For the $b = -a$ setup, one can use a smaller value of a as in the $b = 0$ setup, as discussed in Sec. IV.

non-interacting solution. The calculation has been carried out with two attached chains of $L = 30$ lattice sites each. We did not observe changes for higher bath sizes up to $L = 40$, but could not reach high enough expansion orders for chains longer than $L = 40$. We computed $N = 2500$ moments using a scaling constant $a = 40D$, which corresponds to the full bandwidth.

The calculation can be accelerated significantly by using the $b = -a$ setup of Sec. IV B and avoiding *linear prediction*. This leads to the same quality of agreement with QMC on the Matsubara axis, but on the real axis, peaks are a bit less pronounced while the pseudogap is still well resolved (Fig. 7). While the study of systems with higher bath sizes increases the computational cost tremendously in the $b = 0$ setup, we could easily go to $L = 50$ within the $b = -a$ setup. This did not change the results. Computation times varied from 1.2 h per iteration for $L = 30$, over 3 h for $L = 40$ to around 10 h for the $L = 50$ calculation. We computed $N = 450$ moments using a scaling of $a = 15D$ in all cases.

B. Single-site two-orbital DMFT

In the following, we apply CheMPS to the DMFT treatment of the two-orbital Hubbard model

$$\begin{aligned} H = &\sum_{\boldsymbol{k}\nu\sigma} \varepsilon_{\boldsymbol{k}\nu} n_{\boldsymbol{k}\nu\sigma} + U \sum_{i\nu} n_{i\nu\uparrow} n_{i\nu\downarrow} \\ &+ \sum_{i\sigma\sigma'} (U_1 - \delta_{\sigma\sigma'} J)\, n_{i1\sigma} n_{i2\sigma'} \\ &+ \frac{J}{2} \sum_{i\nu\sigma} c^\dagger_{i\nu\sigma} (c^\dagger_{i\bar{\nu}\bar{\sigma}} c_{i\nu\bar{\sigma}} + c^\dagger_{i\nu\bar{\sigma}} c_{i\bar{\nu}\bar{\sigma}}) c^\dagger_{i\bar{\nu}\sigma} \end{aligned} \tag{30}$$

on the Bethe lattice. We study a parameter regime close to the Metal-Insulator phase transition. This regime is computationally particularly expensive and we had to use a logarithmic discretization to reach Chebyshev expansion orders at which spectral functions are completely converged with respect to expansion order and system size. The linear discretization was feasible in the case of the VBDMFT studied in the previous section, as there, we faced a smaller entanglement entropy production during Chebyshev iterations.

Using a logarithmic discretization is not necessary for CheMPS. But as it leads to exponentially decaying hopping constants, it gives rise to three advantages: (i) One can use smaller scaling constants a as the many-body bandwidth is considerably reduced due to the exponentially small value of most hopping constants in the system. (ii) One faces a smaller entanglement entropy production: at the edges of the bath chains (far away from the impurity), hopping constants are exponentially small, and application of H therefore creates much less entanglement than in the case in which a linear discretization is used. In (14a), the action of H' on $|t_{n-1}\rangle$ is then only a small perturbation for most parts of the system, and the recursion is therefore dominated by the second term $|t_{n-2}\rangle$. Entanglement therefore builds up only in the region where it is relevant, that is, in the vicinity of the impurity. Hence, matrix dimensions grow considerably more slowly when using a logarithmic discretization as compared to a linear discretization. (iii) One faces a faster speed of convergence of the Chebyshev moments as in the linear case: The complexity of the spectral function is considerably reduced when averaging over possible peaks in the high-energy structure of the spectral function, as is done when using a logarithmic grid. The as-

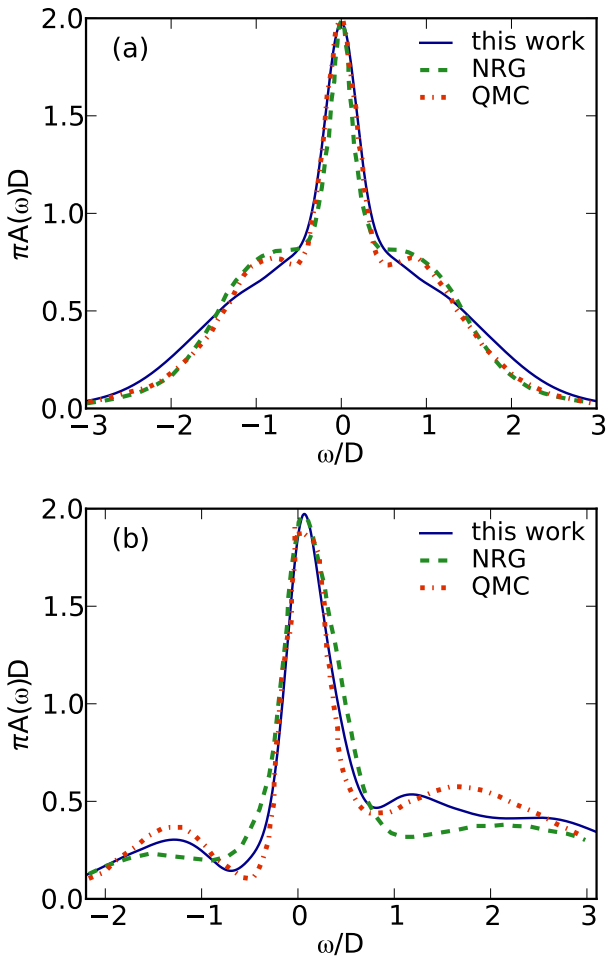

FIG. 8. (Color online) Spectral function for the two-band Hubbard model. Panel (a): $U/D = 1.6$, $n = 2$ (half filling). Panel (b) $U/D = 3.8$, $n = 1$ (quarter filling). In both cases $J = \frac{1}{6}U$, $U' = U - 2J$. We fixed a truncation error $\varepsilon_{\text{compr}} = 10^{-3}$, used a scaling $a = 25D$, computed $N_c = 150$ moments and used linear prediction. To represent the two baths, we used two chains of length $L = 20$ each, obtained with a logarithmic discretization parameter of $\Lambda = 2$, leading to grid energies Λ^{-n} (see e.g. Ref. 10). The NRG calculation was done for temperature $T/D = 0.0025$, the QMC calculation for $T/D = 0.01$. Both should be almost indistinguishable from a $T = 0$ calculation. NRG data from K. Stadler[47] computed with a code of A. Weichselbaum.[48] QMC data from M. Ferrero.[49]

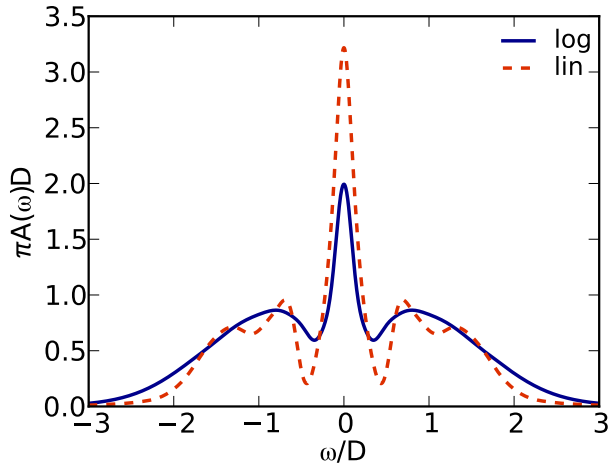

FIG. 9. (Color online) Spectral function for the two-band Hubbard model. The system parameters $U/D = 1.6$, $J/U = \frac{1}{4}$, $U' = U - 2J$, $n = 2$ are very similar to the one in Fig. 8(a). We performed a calculation with linear ("lin", $L = 40$ per bath) and one with logarithmic discretization ("log", $L = 20$ per bath). We fixed a truncation error $\varepsilon_{\text{compr}} = 10^{-3}$. For the calculation with logarithmic discretization, we used a scaling $a = 25D$ and computed $N_c = 300$ moments. For the calculation with linear discretization, we used a scaling of $a = 125D$ and computed $N_c = 1250$ moments. We used linear prediction in all cases. The logarithmic discretization used a discretization parameter $\Lambda = 2$, leading to grid energies Λ^{-n} (see e.g. Ref. 10).

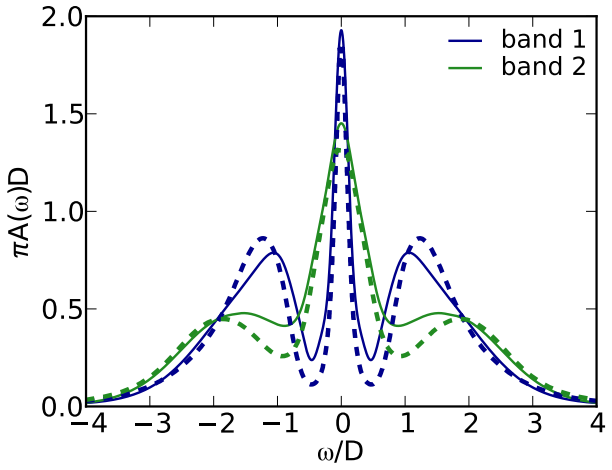

FIG. 10. (Color online) Results for the spectral densities in the two orbitals for $J = 0$. Our results are for $U = 2.6D$, $U' = 1.3D$, $n = 2$ (half filling) and depicted by the solid lines. The reference NRG results[50] are for $U = 2.8D$, $U' = 1.4D$ and depicted by the dashed lines. We had to choose a slightly smaller interaction for a meaningful comparison, as for the parameters of Greger *et al.*[50], we converged, though very slowly, into an insulating solution without central peak. The non-interacting single-particle half-bandwidth of the first band is D, and the one of the second band is $1.4D$. We used two chains of length $L = 20$ each, and a logarithmic discretization parameter of $\Lambda = 2$, leading to grid energies Λ^{-n} (see e.g. Ref. 10).

sociated Chebyshev expansion therefore converges more quickly than in the case of a linear grid.

When using a logarithmic discretization, one has to convolute the resulting spectral function with a Gaussian[46] to average over the finite-size features that originate from the coarse log resolution at high energies.

In Fig. 8, we compare exemplary calculations for the two-band Hubbard model with NRG and analytically continued QMC data. We find good agreement in the regions around the Fermi energy, where the pinning criterion is respected to high accuracy without being enforced. We explain the observed disagreement far away from the Fermi energy with a different specific implementation of the broadening convolution. One DMFT iteration for our calculations took around 20 min running on two 2.5 GHz cores.

In Fig. 9, we study the case of Ref. 35, which is very similar to the one studied in Fig. 8(a). Our results suggest that the data shown in Ref. 35 is not fully converged with respect to computed time in tDMRG, as it does not fulfill the pinning criterion. We face a similar problem when using a linear discretization: For the reachable Chebyshev expansion orders, we do not observe convergence of the central peak height for increasing expansion orders. All peaks, side peaks as well as central peak, increase for increasing expansion order and the pinning criterion is not fulfilled. The additional structure in the Hubbard band, which is not visible in the calculation with the logarithmic discretization, is seen to be similar to the one observed in Ref. 35. One DMFT iteration for the computation that uses a logarithmic grid took 20 min running on two 2.5 GHz cores. For the linear grid this time was 10 h per DMFT iteration.

Finally, we study parameters that lead to a system close to the metal-insulator phase transition. Fig. 10 shows that we obtain satisfactory agreement with NRG data, given the fact that we had to reduce the interaction slightly in order to stay in the metallic phase. This slight quantitative mismatch can possibly again be explained with a differing broadening convolutions in the two calculations. One DMFT iteration took 2 h for the calculation of Fig. 10, when fixing a truncated weight of $\varepsilon_{\text{compr}} = 2 \times 10^{-3}$.

VII. CONCLUSIONS

We solved several DMFT problems with two baths on the real frequency axis with unbiased energy-resolution based on an DMRG impurity solver using Chebyshev polynomials for the representation of spectral functions at moderate numerical effort. DMRG is thereby seen to be a viable alternative for DMFT impurity solvers also

beyond the well-understood single-impurity single-band case.

Technically, it was crucial to apply the adaptive truncation scheme of Sec. III to maintain a modest numerical effort: in all cases, the new scheme gave much better results than the previously employed scheme based on fixed matrix dimensions. Another important way of tuning the calculation is provided by the mapping of the spectrum to the convergence interval of Chebyshev polynomials: The different options to set up a CheMPS calculation can be summarized to yield two alternatives. (i) One uses the $b = 0$ setup and post-processes moments with linear prediction. (ii) One uses the $b = -a$ setup and avoids linear prediction, using simple Jackson damping. Depending on the problem, the first or the second method can be more efficient. The second alternative is computationally much more efficient for cases in which linear prediction is a non-controlled extrapolation scheme, but has problems to resolve sharp peaks at the Fermi edge.

The method presented in this paper can in principle be extended to the case of more than two baths without major changes to the DMFT-DMRG interface and the Chebyshev-based impurity solver as such. However, while two baths can still be modeled by a single chain with the impurity at the center (instead of at the end, as in single-band DMFT), this is no longer possible for three and more baths. This will necessitate a new setup of the DMRG calculation replacing the chain-like by a star-like geometry with the impurity at the center of the star, hence a generalization from a matrix-based to a tensor-based representation at the location of the impurity. It remains to be seen at which numerical cost reliable results on the real frequency axis will be obtainable.

VIII. ACKNOWLEDGEMENTS

FAW acknowledges discussions with C. Hubig and K. Stadler. US acknowledges discussions with M. Ganahl and H.-G. Evertz. FAW and US acknowledge discussions with P. Werner and support by the research unit FOR 1807 of the DFG. O. P. acknowledges support from the ERC Starting Grant 278472–MottMetals. We acknowledge K. Stadler and M. Ferrero for providing the data of their NRG and QMC calculations.

Appendix A: Scaling of Chebyshev Moments with respect to energy scaling

The Chebyshev moments obtained by using two different scalings $H_1' = H/a_1$ and $H_2' = H/a_2$ are from (13) $\mu_n^{a_1} = \sum_i W_i T_n((E_i - E_0)/a_1)$ and $\mu_n^{a_2} = \sum_i W_i T_n((E_i - E_0)/a_2)$. As we consider one-particle operators $c^\dagger$ the weights $W_i = |\langle E_i|c^\dagger|E_0\rangle|^2$ fulfill

$$W_i = 0 \text{ for } E_i \text{ with } |E_i - E_0| \gtrsim W_{\text{single}}, \tag{A1}$$

where W_{single} is the single-particle bandwidth. If the scalings $a = \min(a_1, a_2)$ are chosen large enough, $W_{\text{single}}/a \ll 1$, then

$$\mu^1_{a_1 n} = \mu^2_{a_2 n} \quad \text{if } \frac{a_1 n}{4} \in \mathbb{N} \text{ and } \frac{a_2 n}{4} \in \mathbb{N}. \tag{A2}$$

Proof: If these requirements are met, the eigenvalues E_i with $W_i \neq 0$ are close to the groundstate energy: $x = (E_i - E_0)/a \ll 1$. The Taylor expansion $\arccos(x) = \pi/2 - x - x^3/6 + \ldots$ becomes reliable already when $x \lesssim \frac{1}{2}$, which is fulfilled if a is at least twice the single-particle bandwidth as in all hitherto known applications[27,28,31].

Consider a particular energy $E = E_i - E_0$ for which $W_i > 0$. It holds

$$\begin{aligned}
T_{a_1 n}(E/a_1) &= T_{a_2 n}(E/a_2) \\
\cos(a_1 n \arccos(E/a_1)) &= \cos(a_2 n \arccos(E/a_2)) \\
\cos(a_1 n(\pi/2 - E/a_1)) &\simeq \cos(a_2 n(\pi/2 - E/a_2)) \\
a_1 n(\pi/2 - E/a_1) \bmod 2\pi &\simeq a_2 n(\pi/2 - E/a_2) \bmod 2\pi \\
a_1 n\pi/2 \bmod 2\pi &\simeq a_2 n\pi/2 \bmod 2\pi \\
a_1 n/2 \bmod 2 &\simeq a_2 n/2 \bmod 2.
\end{aligned}$$

A sufficient condition for the last line to hold is that both $a_1 n/2$ and $a_2 n/2$ are multiples of 2, i.e. the statement of (A2).

Appendix B: Chebyshev Moments of Lorentzian and Gaussian

If we fix the shift to be $b = 0$, equation (24) is obtained as follows. As $\mu_n = \sum_i \alpha_i \mu_n^{li}$ we only have to compute the moments for a single Lorentzian, which allows to drop the index i

$$\begin{aligned}
\mu_n^l &= \frac{\eta}{\pi} \int_{-1}^{1} d\omega \frac{\cos(n \arccos(\omega))}{(\omega - \omega_0)^2 + \eta^2} \\
&\simeq \frac{\eta}{\pi} \int_{-1}^{1} d\omega \frac{\cos(n(\frac{\pi}{2} - \omega))}{(\omega - \omega_0)^2 + \eta^2} \\
&= \frac{\eta}{\pi} \int_{-1}^{1} d\omega \frac{\cos(n(\omega + \omega_0'))}{\omega^2 + \eta^2}, \quad \omega_0' = \omega_0 - \frac{\pi}{2} \\
&= \frac{\eta}{\pi} \mathrm{Re} \int_{-1}^{1} d\omega \frac{\exp(in(\omega + \omega_0'))}{\omega^2 + \eta^2} \\
&= \frac{\eta}{\pi} 2\pi i \,\mathrm{Res}\Big(\frac{\cos(in(\omega + \omega_0'))}{\omega^2 + \eta^2}\Big)\Big|_{\omega = i\eta} \\
&= \cos(n(\omega_0 - \frac{\pi}{2}))e^{-n\eta}.
\end{aligned}$$

When closing the integral in the complex plane, we assumed that the Lorentzian concentrates almost all of its weight within $[-1, 1]$, which is a meaningful assumption, as we are calculating with the rescaled frequencies.

For the Gaussian one has

$$A_{\text{Gauss}}(\omega) = \sum_i \alpha_i \frac{1}{\sqrt{2\pi}\sigma_i} e^{-\frac{(\omega-\omega_i)^2}{2\sigma_i^2}},$$
$$\Rightarrow \quad \mu_n^g \simeq \sum_i \alpha_i \cos(n(\omega_i - \frac{\pi}{2}))e^{-(\sigma_i n)^2/2}, \qquad \text{(B1)}$$

as shown by a similar calculation:

$$\begin{aligned}\mu_n^g &= \frac{1}{\sqrt{2\pi}\sigma}\int_{-1}^{1} d\omega\, e^{-\frac{(\omega-\omega_0)^2}{2\sigma^2}} \cos(n \arccos(\omega)) \\ &= \frac{1}{\sqrt{2\pi}\sigma}\int_{-1}^{1} d\omega\, e^{-\frac{\omega^2}{2\sigma^2}} \cos(n(\omega+\omega_0')),\ \omega_0' = \omega_0 - \frac{\pi}{2} \\ &= \frac{1}{\sqrt{2\pi}\sigma}\text{Re}\int_{-1}^{1} d\omega\, e^{-\frac{\omega^2}{2\sigma^2}+in\omega+in\omega_0'} \\ &= \text{Re}\, e^{-\frac{\sigma^2 n^2}{2}+in\omega_0'} = \cos(n(\omega_0 - \frac{\pi}{2}))e^{-\frac{\sigma^2 n^2}{2}}.\end{aligned}$$

From the third to the fourth line, the extension of the integral limits to $\pm\infty$ in order to apply the Gaussian integral formula is well justified, as the Gaussian concentrates all its weight within $[-1, 1]$.

Appendix C: Single-bath impurity calculations

1. Single-impurity Anderson Model

The single impurity Anderson model (SIAM) in its truncated chain representation is

$$H = \sum_{n=0,\sigma}^{L-1} t_n(c_{n\sigma}^\dagger c_{n+1\sigma} + \text{h.c.}) + \sum_{n=0,\sigma}^{L} \varepsilon_i n_{0\sigma} + U n_{0\downarrow} n_{0\uparrow}, \qquad \text{(C1)}$$

with hybridization function[51]

$$\Delta(z) = \cfrac{t_0^2}{z - \varepsilon_1 - \cfrac{t_1^2}{z - \varepsilon_2 - \cfrac{\cdots}{z - \varepsilon_{L-1} - \cfrac{t_{L-1}}{z-\varepsilon_L}}}}. \qquad \text{(C2)}$$

For an infinitely long chain, the continuous version of the SIAM is recovered. The bath density of states is $\Gamma(\omega) = -\frac{1}{\pi}\text{Im}\ \Delta(\omega + i0^+)$. For an infinite homogeneous system with $t_i = t = D/2$, $\varepsilon_i = 0$, $\Gamma(\omega)$ is the semielliptic density of states at half bandwidth D[51]

$$\Gamma(\omega) = \frac{2}{\pi D}\sqrt{1 - (\omega/D)^2}. \qquad \text{(C3)}$$

In the non-interacting case, also the spectral function $A(\omega)$ is semielliptic.

The computation of the spectral function $A(\omega)$ for the SIAM is much less demanding than for most DMFT applications: $A(\omega)$ has only few sharp features, which in addition are well approximated by Lorentzians (Sec. V 1).

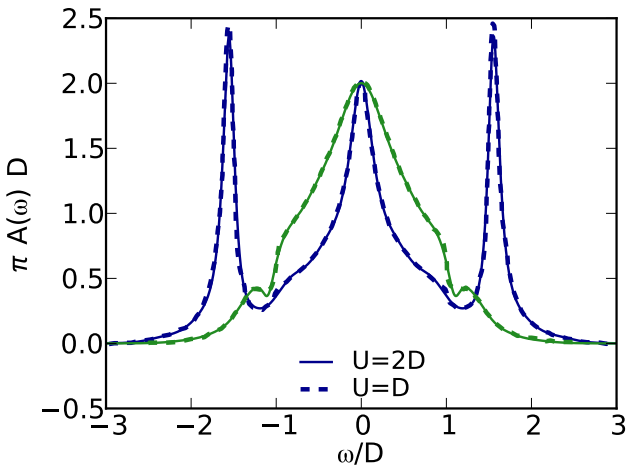

FIG. 11. (Color online) Single Impurity Anderson Model with semi-elliptic density of states of half-bandwidth D. We compute the spectral function with CheMPS allowing a cumulative truncated weight of $\varepsilon_{\text{compr}} = 7 \times 10^{-4}$ and post-process moments with linear prediction (solid lines). These results are compared to data obtained with dynamic DMRG (dashed lines) by Raas *et al.*[39]. We used a fermionic representation of the SIAM on a chain with length $L = 80$.

Hence, linear prediction can be applied and we observe very good agreement with DDMRG data of Raas *et al.*[39] in Fig. 11, confirming results of Ref. 31. For the case $U = D$, we observe a slight disagreement in the region of the shoulders, where the linear prediction predicts two small peaks, whereas DDMRG shows a perfectly flat shoulder. This might point out a failure of linear prediction for the description of this feature. Although this should be of minor importance here, it could matter in other cases.

2. Single-site single-orbital DMFT

The single-site DMFT of the one orbital Hubbard model

$$H = \sum_{\boldsymbol{k}\sigma} \varepsilon_{\boldsymbol{k}} n_{\boldsymbol{k}\sigma} + U \sum_{i\nu} n_{i\uparrow} n_{i\downarrow} \qquad \text{(C4)}$$

is well established[3] and amounts to the determination of the self-consistent parameters $\{t_i, \varepsilon_i\}$ of a SIAM (C1). We give a derivation of the DMFT equations only for the more complicated case of the cluster DMFT (Sec. D), which can easily be reduced to the single site case.

Fig. 12 shows our results for which we fixed a maximum cumulative truncated weight of $\varepsilon_{\text{compr}} = 5 \times 10^{-4}$. For the quite featureless spectral function of Fig. 12(a) ($U = D$), the thermodynamic limit is already obtained for $L = 40$ and one DMFT iteration took 0.3 h. For Fig. 12(b) ($U = 2D$), we needed $L = 80$ and one DMFT iteration took around 3 h. For Fig. 12(b) ($U = 2.4D$) we obtained converged DMFT loops, which violate the

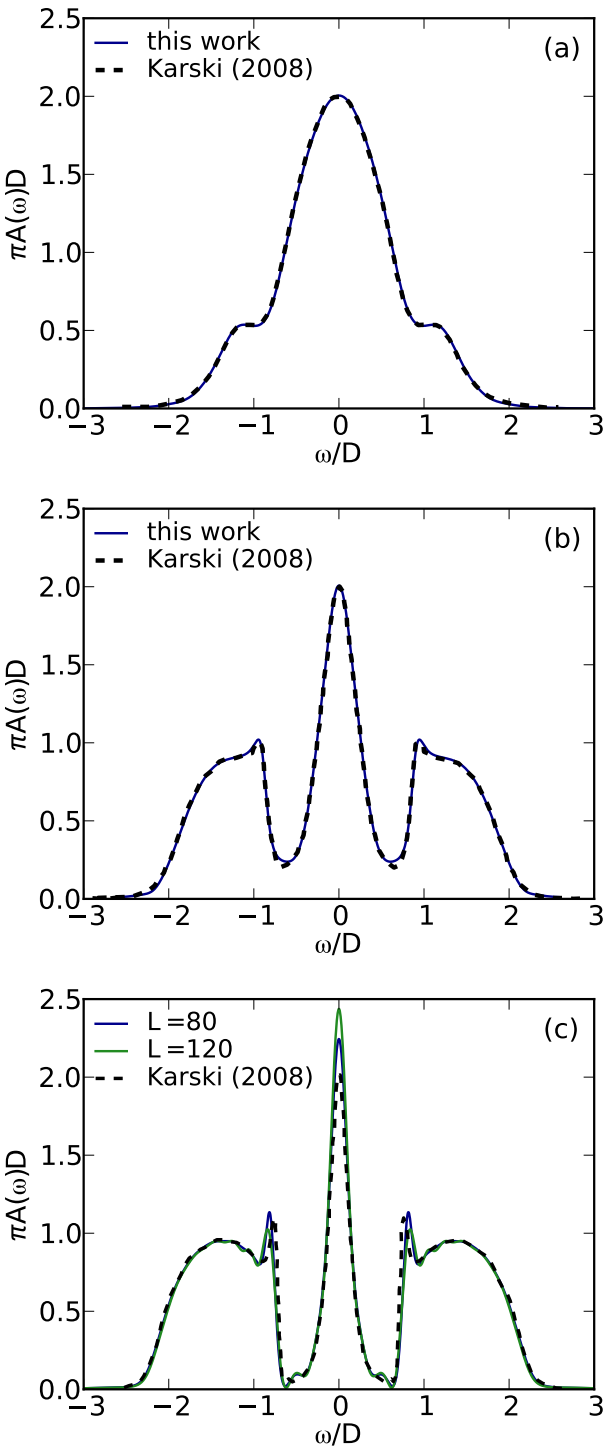

FIG. 12. (Color online) Local density of states within DMFT for the single-band Hubbard model on the Bethe lattice. Computed using CheMPS with an allowed cumulative truncated weight of $\varepsilon_{\mathrm{compr}} = 5 \times 10^{-4}$. Panel (a): $U = D$. Panel (b): $U = 2D$. Panel (c): $U = 2.4D$. We compare our results with data from Karski *et al.*[24].

pinning criterion $A(0) = 2\pi/D$, though. When employing large bath sizes of $L = 100$ and more, we could not reach sufficiently high numbers of Chebyshev moments within reasonable computation times of up to 12 h per DMFT iteration; the linear prediction then overestimates the height of the central peak.

Appendix D: Technical details of VBDMFT

In this appendix, we provide the technical details for the VBDMFT calculation.

1. Self-consistency loop

The Green's function for a patch κ has been introduced in Sec. VI A and reads

$$G_\kappa(z) = \frac{1}{|P_\kappa|} \sum_{\boldsymbol{k} \in P_\kappa} \frac{1}{z + \mu - \varepsilon_{\boldsymbol{k}} - \Sigma_\kappa(z)}. \tag{D1}$$

Within the DCA, one obtains an estimate for $\Sigma_\kappa(z)$ by solving an auxiliary impurity-bath system, the Green's function of which is

$$G^{\mathrm{imp}}_\kappa(z)^{-1} = z + \mu - \Delta_\kappa(z) - \Sigma_\kappa(z), \tag{D2}$$

where the bath is completely characterized by the hybridization function $\Delta_\kappa(z)$.

The problem is then to determine $\Delta_\kappa(z)$ such that the impurity-bath system best approximates the actual lattice environment, which amounts to the *self-consistency* condition

$$G_\kappa(z) = G^{\mathrm{imp}}_\kappa(z). \tag{D3}$$

This equation constitutes a fixed-point problem for the hybridization function $\Delta(z)$ and can hence be solved iteratively, starting with some initial guess, e.g. the non-interacting solution.

Solving the impurity problem for the initial guess of $\Delta(z)$, one obtains $G^{\mathrm{imp}}_\kappa(z)$. From that one obtains the estimate for the self-energy as $\Sigma_\kappa(z) = G^{\mathrm{imp}}_{0\kappa}(z)^{-1} - G^{\mathrm{imp}}_\kappa(z)^{-1}$, or by the method of Bulla *et al.*[52] (we found the latter not to yield advantages for the CheMPS setup). The self-energy is then inserted into (D1) to obtain a new value for $G_\kappa(z)$. Using self-consistency, this defines a new hybridization function by inserting (D3) in (D2):

$$\Delta_\kappa(z) = -G_\kappa(z)^{-1} + z + \mu - \varepsilon_0 - \Sigma_\kappa(z). \tag{D4}$$

In QMC calculations, one defines all quantities on the imaginary axis. In this work as in NRG calculations, we define all quantities on the real axis: the spectral density of the bath is

$$\Gamma(\omega) = -\frac{1}{\pi} \mathrm{Im} \Delta(\omega + i0^+), \tag{D5}$$

which leads to slightly modified version of (D4)

$$\Gamma_\kappa(\omega) = \frac{1}{\pi}\mathrm{Im}(G_\kappa(\omega)^{-1} + \Sigma_\kappa(\omega)). \tag{D6}$$

If one considers ordinary single-site DMFT, all equations remain the same and the momentum patch index κ can be dropped. In a multi-band calculation, the index κ plays the role of the band index. For DMFT carried out for the Bethe lattice, self-consistency can be written as $\Gamma(\omega) = \frac{D^2}{4}A^{\mathrm{imp}}(\omega)$,[3] where $A^{\mathrm{imp}}(\omega) = -\frac{1}{\pi}\mathrm{Im}\, G^{\mathrm{imp}}(\omega + i0^+)$. An iterative solution is particularly simple in this case, as only the spectral function has to be computed and summations over $\boldsymbol{k}$ space are not necessary. In the general case, also the real part of the Green's function is needed. This can either be accessed from the spectral function by the Kramers-Kronig relation or directly from the Chebyshev moments through[27]

$$G^{\mathrm{imp}}(\omega) = -\frac{i}{a}\sum_n w_n(\omega')\mu_n \exp(-in\arccos(\omega')) \tag{D7}$$

where $\omega' \equiv \omega'(\omega)$ is the rescaled frequency defined in (11). The preceding equation should be evaluated slightly away from the real axis $\omega' \to \omega' + i0^+$.

In our computations, we parallelized the independent computations for the particle and the hole part of the Green's (spectral) function, as well as those for different impurity sites.

2. Bath discretization

In order to represent the continuous hybridization function $\Delta(z)$ using a discrete chain, we use the general procedure of Bulla *et al.*[10] (in the notation of Ref. 47) adding details for the special case of the linear discretization.

If we know the hybridization function $\Gamma(\omega)$ (D5) on the real axis, the bath and coupling Hamiltonian can be written as

$$H_b = \int_{-1}^{1} d\varepsilon\, \varepsilon a_\varepsilon^\dagger a_\varepsilon + \int_{-1}^{1} d\varepsilon\, \sqrt{\Gamma(\varepsilon)}(d^\dagger a_\varepsilon + \mathrm{h.c.}) \tag{D8}$$

We discretize the Hamiltonian using a linear discretization of the bath energies

$$\begin{aligned} &I_n = [\epsilon_n, \epsilon_{n+1}], \\ &\epsilon_n = n\Delta\epsilon + \epsilon_0 \text{ for } n \in \{1, 2, \ldots, L_b\}. \end{aligned} \tag{D9}$$

For a given bath size L_b, we fix the free parameters ϵ_0 and $\Delta\epsilon$ by requiring $\int_{\epsilon_0}^{\epsilon_{L_b}} d\omega\Gamma(\omega) = 0.97\int_{-\infty}^{\infty} d\omega\Gamma(\omega)$. This leads to outer interval borders ϵ_0 and ϵ_{L_b} that are close enough to minimize finite-size effects, and far enough apart from each other, to contain almost the complete support of $\Gamma(\omega)$. Starting with an interval $[\epsilon_0^{\mathrm{init}}, \epsilon_{L_b}^{\mathrm{init}}]$ that contains the full integrated weight of $\Gamma(\omega)$, we repeatedly shift the boundaries by a fixed small number to shrink it down to the required size. In a single step, we choose the boundary, that can be shifted with a smaller reduction of the total integral weight. The boundary that leads to a higher reduction is left unchanged in this step. When using a logarithmic discretization, we defined the discretization intervals via energies $\epsilon_m \propto \pm\Lambda^{-m}$, where $m \in [1, ..., L_b/2]$.[10] The specific choice of boundaries of the support is not of much importance in this case.

The discretized SIAM then couples to L_b bath states created by $a_n^\dagger$ each of which corresponds to a bath energy interval I_n. One approximates the continuous H_b by the discrete version

$$\begin{aligned} H_b &\simeq \sum_{n=1}^{L_b} \xi_n a_n^\dagger a_n + \sum_{n=1}^{L_b} \gamma_n(d^\dagger a_n + \mathrm{h.c.}). \\ \gamma_n^2 &= \int_{I_n} d\varepsilon\, \Gamma(\varepsilon), \quad \xi_n = \frac{1}{\gamma_n^2}\int_{I_n} d\varepsilon\, \varepsilon\Gamma(\varepsilon). \end{aligned}$$

In order to use an MPS representation, one has to map the preceding Hamiltonian on a chain Hamiltonian. This is done using the Lanczos algorithm with high-precision arithmetics for the diagonal quadratic matrix $(\xi_n\delta_{nm})_{n,m=1}^{L_b}$ applied to the initial vector $(\gamma_n)_{n=1}^{L_b}$. After L_b Lanczos iterations one obtains the site potentials ε_i as the diagonal of the tridiagonal Lanczos matrix, and the hopping terms as the side-diagonal entries t_i. The hopping term from the impurity site to the first bath chain site is the square root of the total hybridization magnitude $t_0^2 = \sum_n \gamma_n^2 = \int d\varepsilon\Gamma(\varepsilon)$. With these definitions, the final chain Hamiltonian reads

$$H_b \simeq \sum_{i=0}^{L_b} t_i(c_{i+1}^\dagger c_i + \mathrm{h.c.}) + \sum_{i=1}^{L_b} \varepsilon_i c_i^\dagger c_i, \tag{D10}$$

where the impurity site is the first site of the chain $c_0^\dagger \equiv d^\dagger$.

An alternative method to directly obtain the bath parameters by truncating the continued fraction expansion of the hybridization function as put forward by Karski *et al.*[24], did not show any advantages but led to equivalent results. As the method of Karski *et al.*[24] leads to hopping energies that converge to a constant far away from the impurity, while the linear discretization scheme leads to polynomially decreasing hopping energies, the linear discretization method leads to a smaller many-body bandwidth. This allows to use smaller rescaling values in CheMPS.

3. Finding the ground-state

The first problem to solve is finding the ground state of the model Hamiltonian.

a. *Initializing the wave function*

For the two-chain layout (29) of the model, the following problem arises: the chemical potential of both chains

can be strongly different, in which case the particle numbers on the left $N_{\kappa=+}$ and the right $N_{\kappa=-}$ chain may be strongly different. Note that the Hamiltonian of (29) commutes with $N_{\kappa=+}$ and $N_{\kappa=-}$, as the chains are merely coupled by an interaction, not a hopping term. If starting a DMRG groundstate search with a global random state for such a system, convergence can be expected to be very slow, as the local optimization does not pick up the global potential variation. Even worse, the absence of an hopping term between the two chains prevents that during minimization the particle numbers in the left $N_{\kappa=+}$ and the right $N_{\kappa=-}$ chain change. This can in principle be compensated by choosing White's *mixing factor*[53] to be large when starting to sweep, reducing it when being close to convergence. But still we found it impossible to implement a reliable automatized groundstate search under these circumstances.

The problem can be solved by using a $U = 0$ solution as initial guess for the groundstate search. One should realize that the partition between N_- and $N_+ = N - N_-$ (where N is the total particle number) only weakly depends on the interaction U: The total potential and hopping energies scale with the bath length, whereas the interaction energy is a single-site quantity. Given the system parameters $\{\varepsilon_{\kappa i}\}$ and $\{t_{\kappa i}\}$ for each chain κ, we diagonalize the $L = L_b + 1$ dimensional tridiagonal single-particle representation of a single chain with its associated impurity site. This gives us the particle sectors $N_\pm$ of the groundstate of each subsystem. The $U = 0$ estimate for the total particle number sector is $N = N_+ + N_-$, as in this case both subsystems are uncoupled. Given an initial guess for the chemical potential μ, one should initialize a wave function that fulfills the $U = 0$ estimates for N and N_+/N_-.

b. *Finding the correct symmetry sector*

As the DMFT is grand-canonical, one still needs to solve the problem of finding the correct particle number sector for the DMRG calculation. This can be greatly accelerated using the $U = 0$ estimate for N, which constitutes a *rigorous* upper bound for the particle number in the interacting system. For a given μ one can therefore use a bisection search, starting with N, $N - \Delta N$ and $N - 2\Delta N$. In case $N - 2\Delta N$ yields the lowest energy estimate, one has to extend the search regime to lower values of N. If N or $N - \Delta N$ yield the lowest energy, one can continue the ordinary bisection search. For typical interaction values, $\Delta N/N = 0.05$ is a meaningful choice. If searching for the maximum energy state, which is necessary if one wants to determine the full many-body bandwidth $W = E_{\max} - E_0$, one searches for the groundstate of $-H$. In this case the interaction between electrons becomes attractive, and the $U = 0$ solution for the particle number sector of $|E_{\max}\rangle$ becomes a rigorous lower bound for the interacting system.

Having found the correct symmetry sector together with its groundstate for a given value of μ, one has to check whether the requirements for the local impurity densities are fulfilled

$$n - \sum_\kappa \langle c_\kappa^\dagger c_\kappa \rangle \stackrel{?}{=} 0. \tag{D11}$$

To find the correct value of the chemical potential, a simple update of the chemical potential μ with the residuum of (D11) is usually not sufficient to achieve convergence. Instead, we use this method until we found a lower and upper bound for μ and then use a bisection again.

In some cases, the algorithm has to break its search before reaching the required tolerance. This is when the desired chemical potential lies directly on the boundary which separates two different particle number sectors. If this is the case, due to the discrete nature of our model, no solution can be found. Such a case is typically detected by observing oscillations in the residuum of (D11).

When setting up the groundstate search naively, it can easily take most of the computation time of the calculation. Using the procedures just described, it usually takes only a negligible few percent of the total computation time.

4. Definition of the model Hamiltonian

In the following, we outline the standard procedure that eliminates the high-energy contributions in the hybridization function.

We want to represent the non-interacting patch Green's function

$$G_{0\kappa}(z) = \frac{1}{|P_\kappa|} \sum_{\kappa \in P_\kappa} \frac{1}{z + \mu - \varepsilon_{\boldsymbol{k}}}, \tag{D12}$$

by an impurity model with Green's function $G_{0\kappa}^{\mathrm{imp}}(z) = \frac{1}{z+\mu-\Delta(z)}$, such that

$$G_{0\kappa}(z) = G_{0\kappa}^{\mathrm{imp}}(z). \tag{D13}$$

When defining the bath hybridization function naively via

$$\Delta_\kappa(z) = z + \mu - G_{0\kappa}^{-1}(z), \tag{D14}$$

one observes that $\Delta_\kappa(z) \to \bar{t}_\kappa$ for $|z| \to \infty$, when expanding for high values of $|z|$, as

$$G_{0\kappa}(z) = \frac{1}{z+\mu}\left(1 + \frac{\bar{t}_\kappa}{z+\mu} + \mathcal{O}(z^{-1})\right), \tag{D15a}$$

$$G_{0\kappa}^{-1}(z) = z + \mu - \bar{t}_\kappa + \mathcal{O}(z^{-1}), \tag{D15b}$$

where $\bar{t}_\kappa = \frac{1}{|P_\kappa|}\sum_{k \in P_\kappa} \varepsilon_k$.

This means that the corresponding spectral density of the bath $\Gamma(\omega) = -\frac{1}{\pi}\mathrm{Im}\,\Delta(\omega + i0^+)$ has contributions at arbitrarily high energies and the discretization procedure

that maps $\Gamma(\omega)$ onto the discrete bath Hamiltonian H_b must fail.

This problem is solved by defining an impurity model at a shifted chemical potential $\mu \to \mu - \bar{t}_\kappa$. In the hybridization function of this shifted impurity model

$$\Delta_\kappa(z) = z + \mu - \bar{t}_\kappa - G_{0\kappa}^{-1}(z), \tag{D16}$$

the constant $\bar{t}_\kappa$ in the high-energy expansion of $G_{0\kappa}^{-1}(z)$ (D15b) cancels out. It therefore approaches zero for $|z| \to \infty$ while still fulfilling (D13) for $G_{0\kappa}^{\mathrm{imp}}(z) = \frac{1}{z+\mu-\bar{t}_\kappa-\Delta(z)}$. As $\bar{t}_\kappa$ is a simple constant shift of the chemical potential, one can as well incorporate it into the Hamiltonian description of the impurity model, as done in (29).

[1] W. Metzner and D. Vollhardt, Physical Review Letters **62**, 324 (1989).
[2] A. Georges and G. Kotliar, Phys. Rev. B **45**, 6479 (1992).
[3] A. Georges, G. Kotliar, W. Krauth, and M. J. Rozenberg, Rev. Mod. Phys. **68**, 13 (1996).
[4] G. Kotliar, S. Savrasov, K. Haule, V. Oudovenko, O. Parcollet, and C. Marianetti, Reviews of Modern Physics **78**, 865 (2006).
[5] T. Maier, M. Jarrell, T. Pruschke, and M. Hettler, Rev. Mod. Phys. **77**, 1027 (2005).
[6] E. Gull, A. J. Millis, A. I. Lichtenstein, A. N. Rubtsov, M. Troyer, and P. Werner, Rev. Mod. Phys. **83**, 349 (2011).
[7] A. Rubtsov, V. Savkin, and A. Lichtenstein, Phys. Rev. B **72**, 035122 (2005).
[8] E. Gull, P. Werner, O. Parcollet, and M. Troyer, EPL (Europhysics Letters) **82**, 57003 (2008).
[9] P. Werner, A. Comanac, L. de' Medici, M. Troyer, and A. Millis, Physical Review Letters **97** (2006), 10.1103/physrevlett.97.076405.
[10] R. Bulla, T. Costi, and T. Pruschke, Rev. Mod. Phys. **80**, 395 (2008).
[11] M. Caffarel and W. Krauth, Phys. Rev. Lett. **72**, 1545 (1994).
[12] M. Granath and H. U. R. Strand, Phys. Rev. B **86**, 115111 (2012).
[13] Y. Lu, M. Höppner, O. Gunnarsson, and M. W. Haverkort, ArXiv , 1402.0807 (2014), 1402.0807.
[14] A. K. Mitchell, M. R. Galpin, S. Wilson-Fletcher, D. E. Logan, and R. Bulla, Phys. Rev. B **89**, 121105 (2014).
[15] S. R. White, Phys. Rev. Lett. **69**, 2863 (1992).
[16] U. Schollwöck, Rev. Mod. Phys. **77**, 259 (2005).
[17] U. Schollwöck, Annals of Physics **326**, 96 (2011).
[18] K. A. Hallberg, Phys. Rev. B **52**, R9827 (1995).
[19] D. García, K. Hallberg, and M. Rozenberg, Phys. Rev. Lett. **93**, 246403 (2004).
[20] P. E. Dargel, A. Wöllert, A. Honecker, I. P. McCulloch, U. Schollwöck, and T. Pruschke, Phys. Rev. B **85**, 205119 (2012).
[21] F. A. Wolf, unpublished (2013).
[22] T. Kühner and S. White, Phys. Rev. B **60**, 335 (1999).
[23] E. Jeckelmann, Physical Review B **66** (2002), 10.1103/PhysRevB.66.045114.
[24] M. Karski, C. Raas, and G. S. Uhrig, Phys. Rev. B **77**, 075116 (2008).
[25] M. Karski, C. Raas, and G. S. Uhrig, Phys. Rev. B **72**, 113110 (2005).
[26] S. Nishimoto and E. Jeckelmann, J. Phys.: Condens. Matter **16**, 613 (2004).
[27] A. Weiße, G. Wellein, A. Alvermann, and H. Fehske, Rev. Mod. Phys. **78**, 275 (2006).
[28] A. Holzner, A. Weichselbaum, I. P. McCulloch, U. Schollwöck, and J. von Delft, Phys. Rev. B **83**, 195115 (2011).
[29] A. Braun and P. Schmitteckert, ArXiv , 1310.2724 (2013), 1310.2724.
[30] A. C. Tiegel, S. R. Manmana, T. Pruschke, and A. Honecker, ArXiv , 1312.6044 (2013), 1312.6044.
[31] M. Ganahl, P. Thunström, F. Verstraete, K. Held, and H. G. Evertz, ArXiv (2014), 1403.1209.
[32] A. J. Daley, C. Kollath, U. Schollwöck, and G. Vidal, J. Stat. Mech.: Theor. Exp. , P04005 (2004).
[33] G. Vidal, Phys. Rev. Lett. **93**, 040502 (2004).
[34] S. R. White and F. A. E., Phys. Rev. Lett. **93**, 076401 (2004).
[35] M. Ganahl, M. Aichhorn, P. Thunström, K. Held, H. G. Evertz, and F. Verstraete, ArXiv , 1405.6728 (2014), 1405.6728.
[36] L. Lin, Y. Saad, and C. Yang, ArXiv (2013), 1308.5467.
[37] J. B. Boyd, *Chebyshev and Fourier Spectral Methods* (Dover Publications, Mineola, New York, 2001).
[38] F. Verstraete and J. Cirac, Phys. Rev. B **73**, 094423 (2006).
[39] C. Raas, G. S. Uhrig, and F. B. Anders, Phys. Rev. B **69**, 041102 (2004).
[40] W. H. Press, S. A. Teukolsky, W. T. Vetterling, and B. P. Flannery, *Numerical Recipes 3rd Edition: The Art of Scientific Computing*, 3rd ed. (Cambridge University Press, New York, NY, USA, 2007).
[41] S. White and I. Affleck, Phys. Rev. B **77**, 134437 (2008).
[42] T. Barthel, U. Schollwöck, and S. R. White, Phys. Rev. B **79**, 245101 (2009).
[43] R. N. Silver and H. Röder, Phys. Rev. E **56**, 4822 (1997).
[44] M. Ferrero, P. Cornaglia, L. De Leo, O. Parcollet, G. Kotliar, and A. Georges, Physical Review B **80**, 064501 (2009).
[45] M. Ferrero, O. Parcollet, A. Georges, G. Kotliar, and D. N. Basov, Physical Review B **82**, 054502 (2010).
[46] A. Weichselbaum and J. von Delft, Phys. Rev. Lett. **99**, 076402 (2007).
[47] K. Stadler, *Towards exploiting non-abelian symmetries in the Dynamical Mean-Field Theory using the Numerical Renormalization Group*, Master's thesis, LMU Munich (2013).
[48] A. Weichselbaum, Annals of Physics **327**, 2972 (2012).
[49] M. Ferrero, Private Communication.
[50] M. Greger, M. Kollar, and D. Vollhardt, Physical Review

Letters **110**, 046403 (2013).
[51] C. Raas, *Dynamic Density-Matrix Renormalization for the Symmetric Single Impurity Anderson Model*, Ph.D. thesis, University of Cologne (2005).
[52] R. Bulla, A. C. Hewson, and T. Pruschke, Journal of Physics: Condensed Matter **10**, 8365 (1998).
[53] S. R. White, Phys. Rev. B **72**, 180403 (2005).